



# Virtual Formation Method for Precise Autonomous Absolute Orbit Control

S. De Florio\*

*University of Glasgow, Glasgow, Scotland G12 8QQ, United Kingdom*

S. D'Amico†

*DLR, German Aerospace Center, Wessling 82234, Germany*

and

G. Radice‡

*University of Glasgow, Glasgow, Scotland G12 8QQ, United Kingdom*

DOI: 10.2514/1.61575

This paper analyzes the problem of precise autonomous orbit control of a spacecraft in a low Earth orbit. Autonomous onboard orbit control means that the spacecraft maintains its ground track close to a reference trajectory, without operator intervention. The problem is formulated as a specific case of two spacecraft in formation in which one, the reference, is virtual and affected only by the Earth's gravitational field. A new parametrization, the relative Earth-fixed elements, is introduced to describe the relative motion of the two spacecraft's subsatellite points on the Earth surface. These relative elements enable the translation of absolute-into-relative orbit-control requirements and the straightforward use of modern control-theory techniques for orbit control. As a demonstration, linear and quadratic optimum regulators are designed and compared, by means of numerical simulations, with an analytical autonomous orbit-control algorithm that has been validated in flight. The differences of the numerical and analytical control methods are identified and discussed.

## Nomenclature

$A$	=	spacecraft reference area, $\text{m}^2$
$\mathbf{A}$	=	dynamic model matrix, $\text{s}^{-1}$
$a$	=	semimajor axis, m
$\mathbf{B}$	=	control matrix
$\mathbf{C}$	=	output matrix
$C_D$	=	drag coefficient
$e$	=	eccentricity
$e_j$	=	eccentricity vector component
$\mathbf{G}$	=	gain matrix
$\mathbf{G}_d$	=	disturbance gain matrix
$g_j$	=	gain
$i$	=	inclination, rad
$J_2$	=	geopotential second-order zonal coefficient
$m$	=	spacecraft mass, kg
$n$	=	reference spacecraft mean motion, $\text{rad/s}$
$R_E$	=	Earth's equatorial radius, m
$s_j$	=	characteristic root
$\mathbf{T}$	=	coordinates transformation matrix
$t$	=	time, s
$u$	=	argument of latitude, rad
$\bar{u}$	=	constant value of argument of latitude, rad
$v$	=	spacecraft velocity, $\text{m/s}$
$\Delta h$	=	altitude difference, m
$\Delta v_j$	=	impulsive maneuver velocity increment component, $\text{m/s}$
$\delta a$	=	relative semimajor axis

Received 27 December 2012; revision received 3 June 2013; accepted for publication 3 June 2013; published online 5 February 2014. Copyright © 2013 by the American Institute of Aeronautics and Astronautics, Inc. All rights reserved. Copies of this paper may be made for personal or internal use, on condition that the copier pay the \$10.00 per-copy fee to the Copyright Clearance Center, Inc., 222 Rosewood Drive, Danvers, MA 01923; include the code 1533-3884/14 and \$10.00 in correspondence with the CCC.

\*Ph.D. Candidate, Space Advanced Research Team, School of Engineering; s.de-florio.1@research.gla.ac.uk.

†Research Lead, GSOC/Space Flight Technology, Münchner Straße 20.

‡Reader (Aerospace Sciences), Space Advanced Research Team, School of Engineering.

$\delta e$	=	relative eccentricity vector amplitude
$\delta e_j$	=	relative eccentricity vector component
$\delta \mathcal{F}$	=	relative Earth-fixed elements vector
$\delta h$	=	normalized altitude difference
$\delta i$	=	relative inclination vector amplitude, rad
$\delta i_j$	=	relative inclination vector component, rad
$\delta \kappa$	=	relative orbital elements vector
$\delta L_j$	=	phase difference vector component, rad
$\delta \mathbf{r}$	=	normalized relative position vector
$\delta r_j$	=	component of normalized relative position vector
$\delta u$	=	relative argument of latitude, rad
$\delta \mathbf{v}$	=	normalized relative velocity vector
$\delta v_j$	=	component of normalized relative velocity vector
$\epsilon$	=	normalized relative orbital elements vector, m
$\eta$	=	normalized altitude
$\kappa$	=	mean orbital elements vector
$\lambda$	=	longitude, rad
$\mu$	=	Earth's gravitational coefficient, $\text{m}^3/\text{s}^2$
$\xi$	=	thrusters execution error, %
$\rho$	=	atmospheric density, $\text{kg/m}^3$
$\phi$	=	relative perigee, rad
$\varphi$	=	latitude, rad
$\Omega$	=	right ascension of the ascending node, rad
$\dot{\Omega}$	=	secular rotation of the line of nodes, $\text{rad/s}$
$\omega$	=	argument of periapsis, rad
$\omega_E$	=	Earth's rotation rate, $\text{rad/s}$
$\theta$	=	relative ascending node, rad
$\mathbb{R}^-$	=	set of negative real numbers
$\mathbb{R}^+$	=	set of positive real numbers
$\mathbb{Z}$	=	set of integer numbers

## Subscripts

$c$	=	closed-loop
$d$	=	disturbance
$E$	=	Earth
$g$	=	gravity
$N$	=	cross-track
$R$	=	radial
$\mathcal{R}$	=	reference orbit

$r$  = reduced  
 $T$  = along-track

#### Superscripts

$T$  = vector transpose

## I. Introduction

A N AUTONOMOUS orbit-control system can fulfil very strict control requirements on different orbit parameters in real time and with a significant reduction in flight dynamics ground operations [1]. In the last two decades, several studies on the autonomous orbit control of satellites in a low Earth orbit (LEO) have been conducted [2–8]. The TacSat-2 [9], Demeter [10], and autonomous orbit-keeping (AOK) PRISMA [11] in-flight experiments represent milestones in demonstrating that this technology has now reached a sufficient level of maturity to be applied routinely to LEO missions. The next step is to define a general and rigorous formalization of the autonomous orbit-control problem and explore new control methods. This paper analyzes the problem of autonomous absolute orbit control as a specific case of two spacecraft in formation in which one, the reference, is virtual and is affected only by the Earth's gravitational field. The control actions are implemented by means of in-plane and out-of-plane velocity increments. A new parametrization, the relative Earth-fixed elements (REFEs), analogous to the relative orbital elements (ROEs) [12–14], is introduced to describe the relative motion of the real and reference subsatellite points on the Earth surface. The REFEs allow the general formalization of the absolute orbit-control requirements, which are usually expressed through specific Earth-fixed operational parameters such as altitude deviation, phase difference, etc. [15]. A direct mapping between REFE and ROE enables the direct translation of absolute into relative orbit-control requirements. By means of this new formalization, the deviation between the actual and the reference nominal orbit [16] can be defined in an Earth-fixed coordinate system analogous to the orbital frame [17]. This approach allows moreover the straightforward use of modern control-theory techniques for orbit control. Three types of control algorithms are compared. The first is the one used in the AOK [3,11] on the PRISMA [18,19] mission. The AOK controller adopts a guidance law for the orbital longitude of the ascending node and implements an analytical feedback control algorithm using along- and anti-along-track velocity increments. The second and third controllers are the linear and the quadratic optimum regulators from modern control theory [20,21]. This research finds its natural place and exploitation in the steadily increasing orbit-control accuracy requirements for current and future Earth observation missions such as TerraSAR-X [16,22] or Sentinel-1 [23], whose nominal frozen repeat cycle orbits have very strict control requirements within an orbital tube defined in an Earth-fixed frame.

Following a thorough theoretical explanation of the concepts just mentioned, the final part of this paper is dedicated to the presentation of numerical simulations in which the different types of control paradigms are compared. As a case study, the spacecraft MANGO of the PRISMA formation is used because this research is based on the experience and flight data acquired during that mission. The control algorithm implementation used for this research is, in fact, grounded on the expertise gained in the realization of the PRISMA mission navigation and control flight software [24]. The simulation results are evaluated from a performance and operational point of view to formulate a first conclusion about the advantages and disadvantages of the control techniques considered here. The DLR, German Aerospace Center/German Space Operations Center formation-flying simulation platform [25] is used to perform the analyses in a test environment very representative of reality. This test platform includes an orbit propagator and control flight software, and it simulates actuators and navigation errors.

## II. Virtual Formation Model: Parametrization

### A. Relative Orbital Elements

The absolute orbit-control system design can be formulated as the control problem of two spacecraft in formation in which one is virtual and not affected by nongravitational orbit perturbations. The most appropriate parametrization to represent the relative motion of the real spacecraft with respect to the reference is the set of relative orbital elements (ROEs) [26], shown in Eq. (1), where the subscript  $\mathcal{R}$  refers to the reference orbit:

$$\delta\kappa = \begin{pmatrix} \delta a \\ \delta e_x \\ \delta e_y \\ \delta i_x \\ \delta i_y \\ \delta u \end{pmatrix} = \begin{pmatrix} (a - a_{\mathcal{R}})/a_{\mathcal{R}} \\ e_x - e_{x\mathcal{R}} \\ e_y - e_{y\mathcal{R}} \\ i - i_{\mathcal{R}} \\ (\Omega - \Omega_{\mathcal{R}}) \sin i \\ u - u_{\mathcal{R}} \end{pmatrix} \quad (1)$$

These parameters are obtained as a nonlinear combination of the mean orbital elements  $\kappa = (a, e_x, e_y, i, \Omega, u)$  [27–29]. The relative orbit representation of Eq. (1) is based on the relative eccentricity and inclination vectors [30] defined in Cartesian and polar notations as

$$\delta\mathbf{e} = \begin{pmatrix} \delta e_x \\ \delta e_y \end{pmatrix} = \delta e \begin{pmatrix} \cos \phi \\ \sin \phi \end{pmatrix} \quad \delta\mathbf{i} = \begin{pmatrix} \delta i_x \\ \delta i_y \end{pmatrix} = \delta i \begin{pmatrix} \cos \theta \\ \sin \theta \end{pmatrix} \quad (2)$$

The phases of the relative  $\mathbf{e}/\mathbf{i}$  vectors are termed relative perigee  $\phi$  and relative ascending node  $\theta$  because they characterize the relative geometry and determine the angular locations of the perigee and ascending node of the relative orbit. The normalized position  $\delta\mathbf{r} = (\delta r_R \delta r_T \delta r_N)^T/a_{\mathcal{R}}$  and velocity  $\delta\mathbf{v} = (\delta v_R \delta v_T \delta v_N)^T/(na_{\mathcal{R}})$  vectors of the spacecraft relative to the reference orbit in the RTN orbital frame ( $\mathbf{R}$  pointing along the orbit's radius,  $\mathbf{N}$  pointing along the angular momentum vector, and  $\mathbf{T} = \mathbf{N} \times \mathbf{R}$  pointing in the direction of motion for a circular orbit) can be described through the relative orbital elements [26,30] as

$$\begin{pmatrix} \delta\mathbf{r} \\ \delta\mathbf{v} \end{pmatrix} = \begin{pmatrix} \mathbf{T}_p \\ \mathbf{T}_v \end{pmatrix} \delta\kappa = \begin{pmatrix} 1 & -\cos u & -\sin u & 0 & 0 & 0 \\ -(3/2)u & 2\sin u & -2\cos u & 0 & 1/\tan i & 1 \\ 0 & 0 & 0 & \sin u & -\cos u & 0 \\ 0 & \sin u & -\cos u & 0 & 0 & 0 \\ -(3/2) & 2\cos u & 2\sin u & 0 & 0 & 0 \\ 0 & 0 & 0 & \cos u & \sin u & 0 \end{pmatrix} \begin{pmatrix} \delta a \\ \delta e_x \\ \delta e_y \\ \delta i_x \\ \delta i_y \\ \delta u \end{pmatrix} \quad (3)$$

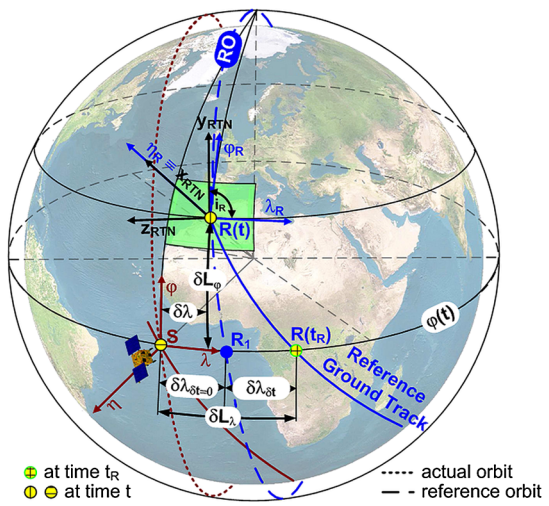


Fig. 1 Geometry of the relative Earth-fixed elements.

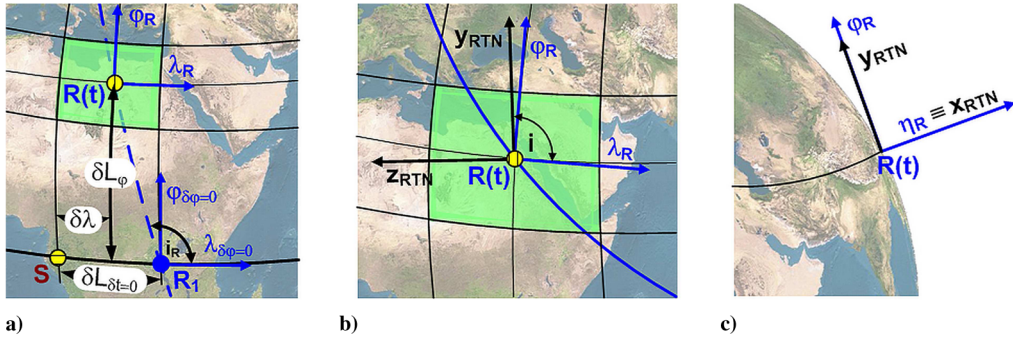


Fig. 2 Earth-fixed and orbital reference frames.

Equation (3) represents the first-order solution of the Clohessy-Wiltshire equations [31] expressed in terms of relative orbital elements.

### B. Relative Earth-Fixed Elements

The constraints on the relative position of the subsatellite points (SSPs) of the real and reference spacecraft and on the difference of their altitudes determine the virtual formation's geometry to be maintained in the **RTN** orbital frame. Referring to Fig. 1, the  $(\lambda\varphi\eta)$  reference frame has the origin in the subsatellite point considered at the altitude of the satellite, the  $\lambda$  axis tangent to the local circle of latitude and pointing eastward, the  $\varphi$  axis tangent to the local meridian and pointing northward, and the  $\eta$  axis pointing along the orbit radius. The relative position of the real and reference SSPs is defined in the  $(\lambda_R\varphi_R\eta_R)$  frame of the reference spacecraft by the phase difference vector  $\delta\mathbf{L} = (\delta L_\lambda, \delta L_\varphi)^T$  and by  $\delta h = \Delta h/a_R$ , the altitude difference normalized to  $a_R$ :

$$\delta L_\lambda = \delta L_{\delta t=0} + \delta L_{\delta t} = (\delta\lambda - \delta\varphi \cot i_R) - \cos \varphi |\omega_E - \dot{\Omega}_R| \delta t \quad (4)$$

$$\delta L_\varphi = \delta\varphi \quad (5)$$

$$\delta h = \delta\eta \quad (6)$$

where  $(\delta\lambda, \delta\varphi, \delta\eta) = (\lambda - \lambda_R, \varphi - \varphi_R, \eta - \eta_R)$ ,  $i_R$  is the reference orbit inclination,  $\varphi$  is the real spacecraft's latitude at time  $t$ ,  $\omega_E = 7.292115 \times 10^{-5} \text{ rad s}^{-1}$  is the Earth's rotation rate,  $\dot{\Omega}_R$  is the secular rotation of the reference orbit line of nodes,  $\delta t = t - t_R$ , and  $t_R$  is the time at which the reference spacecraft passes at latitude  $\varphi$ . Figure 1 depicts the case in which  $t > t_R$ . The phase difference vector's component  $\delta L_\lambda = \delta L_\lambda(\varphi, \delta\lambda, \delta\varphi, \delta t)$  is the distance, normalized to  $a_R$ , of the real and reference ground tracks measured along the  $\lambda$  axis at latitude  $\varphi$ .  $\delta L_\lambda$  is also a function of  $\delta t$  because the real and reference spacecraft pass at latitude  $\varphi$  at different times, and the coordinates systems  $(\lambda_R\varphi_R\eta_R)$  and  $(\lambda\varphi\eta)$  move with the SSPs while the Earth is rotating. The quantity  $\delta L_{\delta t=0}$  is the normalized distance, measured along the  $\lambda$  axis, between the intersection points  $S$  and  $R_1$  of the real and reference orbit projections with the circle of latitude  $\varphi$  at time  $t$  (Figs. 1 and 2). Referring to Fig. 2a, as in the coordinate system  $(\lambda_R\varphi_R\eta_R)$  is  $R_1 \approx (\delta\varphi \cot(\pi - i_R), -\delta\varphi)$ , and  $S = (-\delta\lambda, -\delta\varphi)$ , it results in  $\delta L_{\delta t=0} = R_1 - S \approx \delta\lambda - \delta\varphi \cot i_R$ . The quantity  $\delta L_{\delta t}$  is the normalized distance measured along the  $\lambda$  axis between the

intersection points  $R_1$  and  $R(t_R)$  of the reference orbit projection with the circle of latitude  $\varphi$  at times  $t$  and  $t_R$  (Fig. 1). The minus sign in the second member of Eq. (4) is due to the convention that  $\delta\lambda_{\delta t}$  is positive when  $\delta t$  is negative and vice versa. The time difference  $\delta t$  can be written as  $\delta t = -\delta\varphi n \sin i_R$ , where  $v_\varphi = n \sin i_R$  is the  $\varphi$  component of the velocity of the reference subsatellite point moving on the Earth's surface, and  $n$  is the reference spacecraft mean motion. Hence, Eq. (4) can be written as

$$\delta L_\lambda = \delta\lambda + \left( \frac{|\omega_E - \dot{\Omega}_R| \cos \varphi}{n \sin i_R} - \cot i_R \right) \delta\varphi \quad (7)$$

Because the absolute orbit-control requirements are formulated in terms of REFE [Eqs. (4–6)] but the control is realized in terms of ROE [Eq. (1)], a direct mapping between the two systems is required. Referring to Figs. 2b and 2c for the transformation from **RTN** to  $(\lambda\varphi\eta)$  and using Eqs. (5–7), the REFE vector  $\delta\mathcal{F} = (\delta L_\lambda, \delta L_\varphi, \delta h)^T$  can be mapped into **RTN** coordinates with the transformation

$$\delta\mathcal{F} = \mathbf{T}_{EF} \delta\mathbf{r} \quad (8)$$

$$\mathbf{T}_{EF} = \begin{pmatrix} 0 & \frac{|\omega_E - \dot{\Omega}_R|}{n} \cos \varphi & \left( \frac{|\omega_E - \dot{\Omega}_R|}{n} \cos \varphi \cos i_R - 1 \right) \frac{1}{\sin i_R} \\ 0 & \sin i_R & \cos i_R \\ 1 & 0 & 0 \end{pmatrix} \quad (9)$$

Equation (7) is singular for  $i_R = 0 + k\pi$  (with  $k \in \mathbb{Z}$ ) because, for those values of  $i_R$ , the orbital and equatorial planes are parallel. It is interesting to remark that the term  $\delta L_{\delta t=0}$  of Eq. (4) can be written directly in the **RTN** coordinate system by imposing  $\delta\varphi = \delta r_T \sin i_R + \delta r_N \cos i_R = 0$ , and substituting the solution  $\delta r_T = -\delta r_N \cos i_R / \sin i_R$ , singular for  $i_R = 0 + k\pi$ , in the equation  $\delta\lambda = \delta r_T \cos i_R - \delta r_N \sin i_R$ . Finally, from Eqs. (3) and (8) and substituting  $\cos \varphi = \sqrt{1 - (\sin u \sin i)^2}$ , vector  $\delta\mathcal{F}$  and its time derivative  $d(\delta\mathcal{F})/dt$ , evaluated fixing  $u = \bar{u}$ , can be written in terms of relative orbital elements using the transformation matrix  $\mathbf{T} = \mathbf{T}_{EF} \mathbf{T}_p$ , with  $\mathbf{T}_p$  defined in Eq. (3):

$$\delta\mathcal{F}(\bar{u}, \delta\kappa) = \mathbf{T}(\bar{u}) \delta\mathbf{r} \quad (10)$$

$$\frac{d(\delta\mathcal{F})}{dt} = \mathbf{T}(\bar{u}) \frac{d(\delta\kappa)}{dt} \quad (11)$$

$$\mathbf{T}(u) = \begin{pmatrix} -\frac{3}{2}ut & 2tsu & -2tcu & \frac{su}{si_R}(\tau ci_R - 1) & \left[ \frac{\tau(1-cu)ci_R}{cu} + 1 \right] \frac{cu}{si_R} & \tau \\ -\frac{3}{2}usi_R & 2sus i_R & -2cus i_R & suc i_R & (1-cu)ci_R & si_R \\ 1 & -cu & -su & 0 & 0 & 0 \end{pmatrix} \quad (12)$$

with  $\tau = (|\omega_E - \dot{\Omega}_R|/n)\sqrt{1 - (\sin u \sin i)^2}$ ,  $su = \sin u$ ,  $cu = \cos u$ ,  $si_R = \sin i_R$ , and  $ci_R = \cos i_R$ . Because  $u(t)$  is periodic, the vectorial function  $\delta\mathcal{F}(\bar{u}, \boldsymbol{\delta}\kappa(t))$  is obtained from the function  $\delta\mathcal{F}(u(t), \boldsymbol{\delta}\kappa(t))$  by considering only the subset  $(\bar{u}, \boldsymbol{\delta}\kappa(t))$  of the function's domain  $(u(t), \boldsymbol{\delta}\kappa(t))$ . This is why the term  $(dT/d\bar{u})\delta\kappa = (dT/d\bar{u})d(\bar{u}/dt)\delta\kappa = 0$  does not appear in Eq. (11) if the variation of  $i$  is considered negligible. This procedure is justified by the control design approach explained at the end of Sec. IIIA. Equations (10) and (11) are valid under the assumptions of near-circular orbits, and separations between the real and reference spacecraft are small when compared to the reference orbit radius; see Eq. (3). Table 1 shows the form assumed by the relative Earth-fixed elements when evaluated at the ascending node ( $\bar{u} = 0$ ). The phase difference vector component  $\delta L_\lambda$  at the ascending node is commonly used as operational parameter for the maintenance of phased orbits. If the inclination remains equal to its nominal value, the control of the phase difference at the equator will be the most effective way to monitor the displacement between real and reference ground tracks. It can also be noticed that the maintenance of the altitude deviation  $\delta h$  requires the control of the semimajor axis as well as the eccentricity vector.

### III. Virtual Formation Model: Controller Design

The state-space representation approach is used here for the development of the autonomous orbit control with techniques from modern control theory. In general, the linear model used has the form

$$\dot{\boldsymbol{\epsilon}} = \mathbf{A}\boldsymbol{\epsilon} + \mathbf{B}\Delta\mathbf{v} + \mathbf{x}_d \quad (13)$$

$$\mathbf{y} = \mathbf{C}\boldsymbol{\epsilon} \quad (14)$$

$$\Delta\mathbf{v} = -\mathbf{G}\mathbf{y} - \mathbf{G}_d\mathbf{x}_d \quad (15)$$

where  $\boldsymbol{\epsilon}$  is the state vector;  $\mathbf{A}$  and  $\mathbf{B}$  are the dynamic model and control input matrix, respectively;  $\mathbf{x}_d$  is the modelled state perturbation;  $\Delta\mathbf{v}$  is the impulsive velocity increment vector; and  $\mathbf{G}$  and  $\mathbf{G}_d$  are the output and disturbance gain matrices, respectively. The output vector  $\mathbf{y}$  is composed of relative Earth-fixed elements introduced by Eq. (10).

#### A. Linear Dynamic Model

The state-space model of the orbital motion of the real and reference spacecraft is given by

$$\dot{\boldsymbol{\kappa}} = \tilde{\mathbf{A}}_g(\boldsymbol{\kappa}) + \tilde{\mathbf{A}}_d(\boldsymbol{\kappa}) \quad (16)$$

$$\dot{\boldsymbol{\kappa}}_R = \tilde{\mathbf{A}}_g(\boldsymbol{\kappa}_R) \quad (17)$$

where  $\boldsymbol{\kappa} = (a, e_x, e_y, i, \Omega, u)$  is the mean orbital elements vector.

Vector functions  $\mathbf{A}_g$  and  $\mathbf{A}_d$  [Eqs. (A1) and (A3)] describe the behavior of the mean orbital elements  $\boldsymbol{\kappa}$  under the influence of the  $J_2$  gravitational perturbation and atmospheric drag [29,32]. The mean orbital elements  $\boldsymbol{\kappa}_R$  of the reference spacecraft are affected only by the Earth's gravitational field as they define the nominal trajectory [15,16]. The linearization around  $\boldsymbol{\kappa}_R$  of the difference between Eqs. (16) and (17) yields

$$\frac{d(\delta\boldsymbol{\kappa})}{dt} = \tilde{\mathbf{A}}(\boldsymbol{\kappa}_R)\delta\boldsymbol{\kappa} + \tilde{\mathbf{A}}_d(\boldsymbol{\kappa}_R) \quad (18)$$

where

$$\tilde{\mathbf{A}}(\boldsymbol{\kappa}_R) = \left. \frac{\partial[\tilde{\mathbf{A}}_g(\boldsymbol{\kappa}) + \tilde{\mathbf{A}}_d(\boldsymbol{\kappa})]}{\partial\boldsymbol{\kappa}} \right|_{\boldsymbol{\kappa}_R} \quad (19)$$

is the Jacobian evaluated at  $\boldsymbol{\kappa}_R$  of the vectors sum  $\tilde{\mathbf{A}}_g(\boldsymbol{\kappa}) + \tilde{\mathbf{A}}_d(\boldsymbol{\kappa})$ , and  $\boldsymbol{\delta}\boldsymbol{\kappa}$  is the relative orbital elements vector.

Making the proper modifications to matrix  $\tilde{\mathbf{A}}(\boldsymbol{\kappa}_R)$  for the normalization in  $a_R$  and the introduction of  $\delta i_y$  [Eq. (1)], and adding the control term  $\mathbf{B}(\boldsymbol{\kappa})\Delta\mathbf{v}$ :

$$\dot{\boldsymbol{\epsilon}} = \mathbf{A}(\boldsymbol{\kappa}_R)\boldsymbol{\epsilon} + \mathbf{x}_d + \mathbf{B}(\boldsymbol{\kappa})\Delta\mathbf{v} \quad (20)$$

where  $\mathbf{A}(\boldsymbol{\kappa}_R) = \mathbf{A}_g(\boldsymbol{\kappa}_R) + \mathbf{A}_d(\boldsymbol{\kappa}_R)$  [Eqs. (A2) and (A4)],  $\boldsymbol{\epsilon} = a_R\boldsymbol{\delta}\boldsymbol{\kappa}$  is the relative orbital elements vector [Eq. (1)] normalized to the semimajor axis,  $\mathbf{x}_d$  results from the direct (dyadic) vectors product  $(\tilde{\mathbf{A}}_d(\boldsymbol{\kappa}_R))(1, a_R, a_R, 1, 1, 1)^T$ , and  $\Delta\mathbf{v} = (\Delta v_R, \Delta v_T, \Delta v_N)^T$  is the vector of impulsive velocity increments in the RTN orbital frame. Matrix  $\mathbf{B}(\boldsymbol{\kappa})$  [Eq. (A5)] represents the Gauss variational equations of motion adapted for near-circular nonequatorial orbits [15]. The elements of matrix  $\mathbf{B}(\boldsymbol{\kappa})$  are computed with good approximation [29] using the mean orbital elements. The Gauss equations provide the relationships between the impulsive velocity increments in the RTN orbital frame and the increments of the orbital elements. Equation (20) can be written in the general form

$$\begin{pmatrix} \dot{\boldsymbol{\epsilon}} \\ \dot{\mathbf{x}}_d \end{pmatrix} = \begin{pmatrix} \mathbf{A} & \mathbf{I} \\ \mathbf{0} & \mathbf{A}_0 \end{pmatrix} \begin{pmatrix} \boldsymbol{\epsilon} \\ \mathbf{x}_d \end{pmatrix} + \begin{pmatrix} \mathbf{B} \\ \mathbf{0} \end{pmatrix} \Delta\mathbf{v} \quad (21)$$

Equation (21) is the representation of a tracking system [20] in which the atmospheric drag perturbation vector  $\mathbf{x}_d$  is represented as an additional state variable, the disturbance input, which is assumed to satisfy the model  $\dot{\mathbf{x}}_d = \mathbf{A}_0\mathbf{x}_d$ , and  $\mathbf{I}$  is the  $6 \times 6$  identity matrix. If the feedback controller is designed to compute the control inputs  $\Delta v_j$  always in the same place of the orbit ( $u = \bar{u}$ ),  $\mathbf{x}_d$  can be assumed as constant [Eq. (A3)] (i.e.,  $\mathbf{A}_0 \equiv 0$ ). This design approach stems from the consideration that the implementation of an orbit-control strategy implies the specification not only of the magnitude of the corrective maneuvers but also the in-orbit location that maximizes their efficiency. The choice of the less-expensive maneuver's in-orbit location depends on the operational parameter that has to be controlled. An out-of-plane maneuver  $\Delta v_N$  to change the orbit's inclination, for example, according to the Gauss equations [Eq. (A5)] is most effective if placed at the node ( $\bar{u} = 0$ ) while at the orbit's highest latitude ( $\bar{u} = \pi/2$ ) if  $\Omega$  has to be changed. On the other hand, while the semimajor axis can be changed with an along-track maneuver  $\Delta v_T$  with the same effectiveness anywhere along the orbit, the  $\Delta v_T$  most effective [11] to control  $\delta L_\lambda$  (Table 1) has to be computed at the equator (ascending or descending node) for reasons of symmetry.

#### B. Reduced Model

In case no eccentricity or inclination are to be actively controlled, the model can be reduced to Eq. (22) by considering only the states  $\delta a$ ,  $\delta i_y$ , and  $\delta u$ . The elements  $a_{ij} = a_{gij} + a_{dij}$  are given by Eqs. (A2) and A4. The use of this model allows the design of a linear controller for the relative Earth-fixed elements  $\delta L_\lambda$  and  $\delta L_\varphi$ . The passive control of  $\delta h$  can be achieved by a proper in-orbit placement of the along-track maneuvers as explained in the next section:

$$\begin{aligned} \mathbf{A}_r &= \frac{3}{4} \left( \frac{a}{R_E} \right)^2 \frac{nJ_2}{(1-e^2)^2} \begin{pmatrix} a_{11} & 0 & 0 \\ a_{51} & 0 & 0 \\ a_{61} & 0 & 0 \end{pmatrix} & \boldsymbol{\epsilon}_r &= a_R \begin{pmatrix} \delta a \\ \delta i_y \\ \delta u \end{pmatrix} \\ \mathbf{B}_r &= \frac{1}{n} \begin{pmatrix} 0 & 2 & 0 \\ 0 & 0 & \sin u \\ -2 & 0 & -\sin u / \tan i \end{pmatrix} & \mathbf{x}_{dr} &= -\frac{A}{m} C_D \rho \begin{pmatrix} \sqrt{\mu a} \\ 0 \\ 0 \end{pmatrix} \end{aligned} \quad (22)$$

Table 1 Relative Earth-fixed elements (specific case)

$i_R$	$\bar{u}$	$\delta L_\lambda$	$\delta L_\varphi$	$\delta h$
$i_R$	0	$\delta i_y / \sin i_R + ( \omega_E - \dot{\Omega}_R /n)(\delta u - 2\delta e_y)$	$(\delta u - 2\delta e_y) \sin i_R$	$\delta a - \delta e_x$

In this case, Eqs. (10–12) have the following form:

$$\delta\mathcal{F}(\bar{u}, \boldsymbol{\epsilon}_r) a_{\mathcal{R}} = \mathbf{T}_r(\bar{u}) \boldsymbol{\epsilon}_r \quad (23)$$

$$\frac{d(\delta\mathcal{F})}{dt} a_{\mathcal{R}} = \mathbf{T}_r(\bar{u}) \mathbf{A}_r \boldsymbol{\epsilon}_r \quad (24)$$

$$\mathbf{T}_r(u) = \begin{pmatrix} -\frac{3}{2}u\tau & \left[\frac{\tau(1-cu)c_{i\mathcal{R}}}{cu} + 1\right] \frac{cu}{si\mathcal{R}} & \tau \\ -\frac{3}{2}usi\mathcal{R} & (1-cu)c_{i\mathcal{R}} & si\mathcal{R} \\ 1 & 0 & 0 \end{pmatrix} \quad (25)$$

### C. Linear Control

The linear control law for the system Eq. (21) has the general form [20] of Eq. (15).  $\mathbf{G}$  and  $\mathbf{G}_d$  are the gain matrices, and  $\mathbf{y} = \mathbf{C}\boldsymbol{\epsilon}$  is the system's output. The terms of matrix  $\mathbf{C}$  will be computed from Eq. (12) because the goal of the proposed absolute orbit controller is the maintenance of one or more relative Earth-fixed elements within their control windows. For the closed-loop system to be asymptotically stable, the characteristic roots [20] of the closed-loop dynamics matrix  $\mathbf{A}_c = \mathbf{A} - \mathbf{B}\mathbf{G}\mathbf{C}$  must have negative real parts. This can be accomplished by a suitable choice of the gain matrix  $\mathbf{G}$  if the system is controllable. Once the gains and thus the poles of matrix  $\mathbf{A}_c$  have been set, matrix  $\mathbf{G}_d$  is obtained substituting Eq. (15) in Eq. (20), imposing  $\mathbf{y} = \mathbf{C}\boldsymbol{\epsilon}$  and the steady-state condition  $\dot{\boldsymbol{\epsilon}} = \mathbf{0}$ :

$$\mathbf{G}_d = (\mathbf{C}\mathbf{A}_c^{-1}\mathbf{B})^{-1}\mathbf{C}\mathbf{A}_c^{-1}\mathbf{I} \quad (26)$$

The linear control system is designed by means of pole placement. The choice of which relative Earth-fixed element has to be controlled is determined by the mission requirements, whereas the best place and direction of the orbital maneuvers is also dictated by the Gauss equations [Eq. (A5)]. First, an in-plane orbit-control system will be considered with the single control input ( $\Delta v_T$ ) and two outputs ( $\delta L_\lambda$  and  $d(\delta L_\lambda)/dt$ ), computed at the orbit's ascending node. This is the basic control required for the maintenance of a repeat-track orbit [15]. Second, an in-plane/out-of-plane controller with two control inputs ( $\Delta v_T$  and  $\Delta v_N$ ) and three outputs ( $\delta L_\lambda$ ,  $d(\delta L_\lambda)/dt$ , and  $\delta i_y$ ) is designed. In this case, the in-orbit phasing  $\delta L_\phi$  can be restrained in a control window as well. The design of these regulators will be based on the reduced model [Eq. (22)].

#### 1. In-Plane Control with One Input and Two Outputs

In this case, the design of the feedback system is finalized to control  $\delta L_\lambda$  and  $d(\delta L_\lambda)/dt$ , computed at the ascending node (Table 1), by means of along-track velocity increments. This means that the orbit controller is designed to work only once per orbit at most. The system components are

$$\begin{aligned} \mathbf{A}_r &= \begin{pmatrix} a_{r_{11}} & 0 & 0 \\ a_{r_{21}} & 0 & 0 \\ a_{r_{31}} & 0 & 0 \end{pmatrix} & \boldsymbol{\epsilon}_r &= a_{\mathcal{R}} \begin{pmatrix} \delta a \\ \delta i_y \\ \delta u \end{pmatrix} & \mathbf{B}_r &= \begin{pmatrix} b_1 \\ 0 \\ 0 \end{pmatrix} \\ \mathbf{G} &= (g_1 \ g_2) & \mathbf{G}_d &= (g_0 \ 0 \ 0) & \mathbf{x}_{dr} &= \begin{pmatrix} x_{d1} \\ 0 \\ 0 \end{pmatrix} \end{aligned} \quad (27)$$

with  $a_{r_{11}}, a_{r_{21}}, a_{r_{31}}, b_1 = 2/n$ , and  $x_{d1}$  given by Eq. (22), and  $g_1, g_2 \in \mathbb{R}$ . The output  $\mathbf{y} = \mathbf{C}\boldsymbol{\epsilon}_r$  is

$$a_{\mathcal{R}} \begin{pmatrix} \frac{d(\delta L_\lambda)}{dt} \\ \frac{d(\delta L_\lambda)}{dt} \end{pmatrix} = a_{\mathcal{R}} \begin{pmatrix} 0 & c_{12} & c_{13} \\ c_{21} & 0 & 0 \end{pmatrix} \begin{pmatrix} \delta a \\ \delta i_y \\ \delta u \end{pmatrix} \quad (28)$$

where the terms  $c_{12} = 1/\sin i_{\mathcal{R}}$ ,  $c_{13} = |\omega_E - \dot{\Omega}_{\mathcal{R}}|/n$  and  $c_{21} = a_{r_{21}}/\sin i_{\mathcal{R}} + a_{r_{31}}|\omega_E - \dot{\Omega}_{\mathcal{R}}|/n$  are obtained from Eqs. (23–25) imposing  $\bar{u} = 0$ .

The control input is given by  $\Delta v_T = -(g_1 \delta L_\lambda + g_2 d(\delta L_\lambda)/dt) a_{\mathcal{R}}$ . The objective here is to find the gains  $g_1$  and  $g_2$  that place the poles of the closed-loop dynamic matrix  $\mathbf{A}_c = \mathbf{A}_r - \mathbf{B}_r \mathbf{G} \mathbf{C}$  at the locations desired. The characteristic polynomial of  $\mathbf{A}_c$  is

$$\begin{aligned} |s\mathbf{I} - \mathbf{A}_c| &= s[s^2 + (b_1 c_{21} g_2 - a_{r_{11}})s + b_1(a_{r_{21}} c_{12} + a_{r_{31}} c_{13})g_1] \\ &= s[s^2 + \hat{a}_1(g_2)s + \hat{a}_2(g_1)] \end{aligned} \quad (29)$$

One of the three poles of  $\mathbf{A}_c$  is placed in the origin regardless of the value of the gains. This is due to the fact that the part of the system depending on  $\delta i_y$  is not controllable by  $\Delta v_T$ . Indeed the controllability test matrix of Eq. (30) has rank 2 < 3. However,  $\delta L_\lambda$  can be controlled by means of variations of  $\delta u$ , which compensate the variations of  $\delta i_y$  (Table 1):

$$\mathbf{Q}_{ctr} = (\mathbf{B} \ \mathbf{A}_r \mathbf{B}_r \ \mathbf{A}_r^2 \mathbf{B}_r) = \begin{pmatrix} b_1 & a_{r_{11}} b_1 & a_{r_{11}}^2 b_1 \\ 0 & a_{r_{21}} b_1 & a_{r_{11}} a_{r_{21}} b_1 \\ 0 & a_{r_{31}} b_1 & a_{r_{11}} a_{r_{31}} b_1 \end{pmatrix} \quad (30)$$

The closed-loop poles  $s = (-\hat{a}_1 \pm \sqrt{\hat{a}_1^2 - 4\hat{a}_2})/2$  of Eq. (29) are real (or complex-conjugate) if  $|\hat{a}_1| > 2\sqrt{\hat{a}_2}$  (or  $|\hat{a}_1| < 2\sqrt{\hat{a}_2}$ ) and  $\hat{a}_2 = b_1 c_{21} g_1 > 0$ . If  $\hat{a}_1 > 0$ , the poles are placed on the left of the imaginary axis of the complex plane, and the closed-loop system is stable. These stability conditions impose constraints on the value of the gains as resumed by Table 2. If the poles chosen are complex-conjugate, the contribution of the term  $-g_2(d(\delta L_\lambda)/dt)a_{\mathcal{R}}$  to the control action  $\Delta v_T$  will be negligible because  $a_{\mathcal{R}} d(\delta L_\lambda)/dt$  has an order of magnitude of  $30/86, 400 \text{ m} \cdot \text{s}^{-1}$  [11], and the value of  $g_2$  is limited in the range indicated in the second row of Table 2. This means that to also control  $d(\delta L_\lambda)/dt$ , the poles have to be on the negative real axis because, in this way, a suitably large value of  $g_2$  can be obtained. The gains are related to the poles by the following equation:

$$g_1 = \frac{s_1 s_2}{b_1(a_{r_{21}} c_{12} + a_{r_{31}} c_{13})}, \quad g_2 = \frac{s_1 + s_2 + a_{r_{11}}}{b_1 c_{21}} \quad (31)$$

with  $s_1, s_2 \in \mathbb{R}^-$ . The gain values chosen as a first guess are  $g_1 = \text{sgn}(c_{21}) \Delta v_{T_{sl}} / (a_{\mathcal{R}} \delta L_{\lambda_{MAX}})$  and  $g_2 = \text{sgn}(c_{21}) \Delta v_{T_{dsl}} / (a_{\mathcal{R}} d(\delta L_\lambda)/dt)_{MAX}$ , where  $\Delta v_{T_{sl}}$ ,  $\Delta v_{T_{dsl}}$ ,  $a_{\mathcal{R}} \delta L_{\lambda_{MAX}}$ , and  $(a_{\mathcal{R}} d(\delta L_\lambda)/dt)_{MAX} \in \mathbb{R}^+$  are limits imposed by design, and  $\text{sgn}(c_{21})$  is the sign of  $c_{21}$ . The dynamics of the closed-loop system can be verified and adjusted by computing the poles with Eq. (31), adjusting their placement, and iterating the process. The control input is

$$\Delta v_T = -\mathbf{G}\mathbf{C}\boldsymbol{\epsilon}_r = -(g_2 c_{21} \delta a + g_1 c_{12} \delta i_y + g_1 c_{13} \delta u) a_{\mathcal{R}} \quad (32)$$

The following subsystem of Eq. (27) is considered for the determination of the disturbance gain matrix  $\mathbf{G}_d$  [Eq. (15)]:

$$\frac{d(\delta a)}{dt} a_{\mathcal{R}} = (a_{r_{11}} \delta a) a_{\mathcal{R}} + b_1 \Delta v_T + x_{d1} \quad y = a_{\mathcal{R}} \delta a \quad (33)$$

for which Eq. (26) yields  $g_0 = 1/b_1$ , and then

**Table 2 Gain constraints**

Pole type	$c_{21}(i) > 0$ and $g_1 > 0$	$c_{21}(i) < 0$ and $g_1 < 0$
Real	$g_2 > \frac{a_{r_{11}} + 2\sqrt{\hat{a}_2}}{b_1 c_{21}}$	$g_2 < \frac{a_{r_{11}} + 2\sqrt{\hat{a}_2}}{b_1 c_{21}}$
Complex	$\frac{a_{r_{11}}}{b_1 c_{21}} < g_2 < \frac{a_{r_{11}} + 2\sqrt{\hat{a}_2}}{b_1 c_{21}}$	$\frac{a_{r_{11}} + 2\sqrt{\hat{a}_2}}{b_1 c_{21}} < g_2 < \frac{a_{r_{11}}}{b_1 c_{21}}$

$$\mathbf{G}_d = \begin{pmatrix} \frac{1}{b_1} & 0 & 0 \end{pmatrix} \quad (34)$$

The term  $x_{d1}/b_1$  for a small satellite in a low Earth orbit has an order of magnitude of  $10^{-8}$  m/s and is negligible in the computation of  $\Delta v_T$ . This is not surprising because  $\mathbf{G}_d$  represents the instantaneous effect of the drag and not its integration over time.

The maneuvers have to be computed at the ascending node but can be executed with the same effectiveness in any place along the orbit as they change  $\delta u$  by means of semimajor axis increments [first row of Eq. (A5)]. Nevertheless, the along-track maneuvers can be located [26] to be the most effective on the control of the relative eccentricity vector components  $\delta e_x$  and  $\delta e_y$ . Solving the second and third of the Gauss equations  $\dot{\epsilon} = \mathbf{B}(\kappa)\Delta\mathbf{v}$  in  $u$  and imposing that the effect of the velocity increment  $\Delta v_T$  is decreasing the magnitude of  $\delta e_x$  and  $\delta e_y$ , the eccentricity vector can be passively controlled with a proper in-orbit location [33] of the along-track maneuver:

$$\begin{aligned} u_M &= \arctan\left(\frac{\delta e_y}{\delta e_x}\right) + k\pi, & k = 0 & \text{if } (\delta e_x \Delta v_T) < 0, \\ k &= 1 & \text{if } (\delta e_x \Delta v_T) > 0 \end{aligned} \quad (35)$$

## 2. In-Plane/Out-of-Plane Control with Two Inputs and Three Outputs

In this case, the design of the system is finalized to control the relative Earth-fixed elements  $\delta L_\lambda$  and  $\delta L_\varphi$  at the ascending node by means of along-track and cross-track velocity increments. At the ascending node,  $\delta L_\lambda$  and  $\delta L_\varphi$  are related to each other by the equation  $\delta L_\lambda = k_1 \delta i_y + k_2 \delta L_\varphi$ , where  $k_1$  and  $k_2$  are the values displayed in Table 1. The only chance of controlling  $\delta L_\lambda$  and  $\delta L_\varphi$  at the same time  $\delta L_\varphi$  is thus selecting  $\delta i_y$  as one of the controlled outputs. The velocity increment  $\Delta v_N$  to control  $\delta i_y$  has to be placed at the orbit's highest latitude ( $u = \pi/2$ ) to maximize its effectiveness [fifth row of Eq. (A5)]. The execution of  $\Delta v_T$  will be placed with the rule of Eq. (35). The system components are  $\mathbf{A}_r$  and  $\mathbf{e}_r$  from Eq. (27) and

$$\mathbf{B}_r = \begin{pmatrix} b_1 & 0 \\ 0 & b_2 \\ 0 & 0 \end{pmatrix} \quad \mathbf{G} = \begin{pmatrix} g_1 & g_2 & 0 \\ 0 & 0 & g_N \end{pmatrix} \quad (36)$$

where  $b_1 = 2/n$ ,  $b_2 = \sin u/n$  are given by the first and fifth rows of matrix  $\mathbf{B}$  [Eq. (A5)], and the term of  $\mathbf{B}_r$  relating  $\Delta v_N$  and  $\delta u$  has been omitted by design. The output  $\mathbf{y} = \mathbf{C}\mathbf{e}_r$  is

$$a_{\mathcal{R}} \begin{pmatrix} \frac{\delta L_\lambda}{\delta i_y} \\ \frac{d(\delta L_\lambda)}{dr} \end{pmatrix} = a_{\mathcal{R}} \begin{pmatrix} 0 & c_{12} & c_{13} \\ c_{21} & 0 & 0 \\ 0 & 1 & 0 \end{pmatrix} \begin{pmatrix} \delta a \\ \delta i_y \\ \delta u \end{pmatrix} \quad (37)$$

where  $c_{12}$ ,  $c_{13}$ , and  $c_{21}$  are the same as in Eq. (28). The system is controllable as the rank of the controllability matrix is 3. The characteristic polynomial of  $\mathbf{A}_c = \mathbf{A}_r - \mathbf{B}_r \mathbf{G} \mathbf{C}$  is

$$\begin{aligned} |\mathbf{sI} - \mathbf{A}_c| &= s^3 + (b_1 g_2 c_{21} + b_2 g_N - a_{r1}) s^2 \\ &+ [b_1 g_1 (a_{r21} c_{12} + a_{r31} c_{13}) + b_2 g_N (b_1 g_2 c_{21} - a_{r11})] s \\ &+ a_{r31} c_{13} b_1 b_2 g_1 g_N = s^3 + \hat{a}_1 (g_2, g_N) s^2 \\ &+ \hat{a}_2 (g_1, g_2, g_N) s + \hat{a}_2 (g_1, g_N) \end{aligned} \quad (38)$$

The proper control gains can be found by splitting the problem into two distinct subproblems. The first-guess values of  $g_1$  and  $g_2$  are the same found solving the problem of the previous section. The cross-track maneuver gain is found with the relation  $g_N = a_{\mathcal{R}} \delta i_{y_{\text{MAX}}} / \Delta v_{N_{\text{MAX}}}$ , where  $\delta i_{y_{\text{MAX}}}, \Delta v_{N_{\text{MAX}}} \in \mathbb{R}^+$  are imposed by design. The placement of the closed-loop poles and the dynamic response of the system can then be verified by finding the roots of Eq. (38). The control input is

$$\begin{aligned} \Delta v_T &= [-g_2 c_{21} \delta a - g_1 (c_{12} \delta i_y + c_{13} \delta u)] a_{\mathcal{R}} \\ \Delta v_N &= -g_N \delta i_y a_{\mathcal{R}} \end{aligned} \quad (39)$$

## D. Linear Quadratic Optimum Regulator Control

The linear quadratic optimum regulator (LQR) [20] is best suited for a multiple-input/multiple-output system like that here considered. Here, instead of seeking a gain matrix to achieve specified closed-loop locations of the poles, a gain is sought to minimize a specified cost function  $\Lambda$  expressed as the integral of a quadratic form in the state  $\mathbf{e}$  plus a second quadratic form in the control  $\Delta\mathbf{v}$ :

$$\Lambda = \int_t^T [\mathbf{e}^T(\tau) \mathbf{C}^T \mathbf{Q}_y \mathbf{C} \mathbf{e}(\tau) + \Delta \mathbf{v}^T(\tau) \mathbf{R} \Delta \mathbf{v}(\tau)] d\tau \quad (40)$$

where  $\mathbf{Q} = \mathbf{C}^T(\tau) \mathbf{Q}_y(\tau) \mathbf{C}$  is the  $6 \times 6$  state weighting symmetric matrix,  $\mathbf{Q}_y$  is the weighting matrix of the output  $\mathbf{y} = \mathbf{C}\mathbf{e}$ , and  $\mathbf{R}$  is the  $3 \times 3$  control weighting symmetric matrix. The optimum steady-state [ $T = \infty$  in Eq. (37)] gain matrix  $\mathbf{G}$  for system Eq. (21) is

$$\mathbf{G} = -\mathbf{R}^{-1} \mathbf{B}^T \bar{\mathbf{M}} \quad (41)$$

where  $\bar{\mathbf{M}}$  is the steady-state solution to the Riccati equation

$$\dot{\bar{\mathbf{M}}} = \bar{\mathbf{M}} \mathbf{A} + \mathbf{A}^T \bar{\mathbf{M}} - \bar{\mathbf{M}} \mathbf{B} \mathbf{R}^{-1} \mathbf{B}^T \bar{\mathbf{M}} + \mathbf{Q} = 0 \quad (42)$$

The disturbance gain matrix  $\mathbf{G}_d$  for the case of Eq. (21), in which  $\mathbf{x}_d$  is constant, is given by

$$\mathbf{G}_d = -\mathbf{R}^{-1} \mathbf{B}^T (\mathbf{A}_c^T)^{-1} \bar{\mathbf{M}} \mathbf{I} \quad (43)$$

where  $\mathbf{A}_c = \mathbf{A} - \mathbf{B}\mathbf{G}$  is the closed-loop dynamics matrix,  $\bar{\mathbf{M}}$  is given by Eq. (42), and  $\mathbf{I}$  is the identity matrix. As already remarked in Sec. III.C.1, the term  $\mathbf{G}_d \mathbf{x}_d$  can be neglected. In the performance function defined by Eqs. (40), the quadratic form  $\mathbf{y}^T \mathbf{Q} \mathbf{y}$  represents a penalty on the deviation of the real from the reference orbit, and the weighting matrix  $\mathbf{Q}$  specifies the importance of the various components of the state vector relative to each other. The term  $\Delta \mathbf{v}^T \mathbf{R} \Delta \mathbf{v}$  is instead included to limit the magnitude of the control signal  $\Delta \mathbf{v}$  and to prevent saturation of the actuator. Overall, the gain matrices choice is a tradeoff between control action cost (i.e., small gains to limit propellant consumption and avoid thruster saturation phenomena) and control accuracy (i.e., large gains to limit the excursion of the state from its reference value). The choice of the weighting matrices is done here with the maximum size technique. The aim of this method is to confine the individual states and control actions within prescribed maximum limits given respectively by  $y_{i_{\text{MAX}}}$  and  $\Delta v_{i_{\text{MAX}}}$ . The terms of  $\mathbf{Q}_y$  and  $\mathbf{R}$  will be thus chosen imposing the following equations:

$$Q_{yii} = \frac{k_i}{y_{i_{\text{MAX}}}^2}, \quad Q_{yij} = \frac{k_{ij}}{2y_{i_{\text{MAX}}} y_{j_{\text{MAX}}}}, \quad (44)$$

$$k_{ij} \in \mathbb{R} \quad \text{for } i = 1, 2, 3 \quad \text{and} \quad j = 1, 2, 3$$

$$R_{ii} = \frac{h_i}{\Delta v_{i_{\text{MAX}}}^2}, \quad R_{ij} = \frac{h_{ij}}{2\Delta v_{i_{\text{MAX}}} \Delta v_{j_{\text{MAX}}}}, \quad (45)$$

$$h_{ij} \in \mathbb{R} \quad \text{for } i = R, T, N \quad \text{and} \quad j = R, T, N$$

The choice of diagonal  $\mathbf{Q}_y$  and  $\mathbf{R}$  matrices is usually a good starting point in a trial-and-error design procedure aimed at obtaining the desired properties of the controller.

## IV. Numerical Simulations

Two types of numerical simulations were run to validate and compare the control methods introduced in the previous sections. A first set of simulations was based on an orbit propagation model, which included the gravitational field and a constant atmospheric drag as the orbital perturbations. This is also the perturbation model on which the analytical algorithm of the AOK controller [3,11] is based. By means of these ideal simulations, the performance of the different controllers could be compared under theoretical design

conditions. A second set of simulations was run to compare the behavior of the controllers in a realistic orbit environment. Tables 3–6 display the spacecraft physical parameters, the orbit propagation model, and the sensor, actuators, and navigation models used for the simulations. The propulsion system is characterized by a minimum impulse value (MIV) and a minimum impulse bit (MIB). Consequently, the thrusters can only deliver values of  $\Delta v$ , which are larger than MIV and integer multiples of MIB. Furthermore, the execution error of the thrusters is quantified by the relation  $\xi = |(\Delta v_{\text{real}} - \Delta v_{\text{cmd}})/\Delta v_{\text{cmd}}| \cdot 100$ , where  $\Delta v_{\text{cmd}}$  is the velocity increment commanded by the onboard controller, and  $\Delta v_{\text{real}}$  is the actual velocity increment executed by the propulsion system. Finally, the attitude-control error, which causes thruster misalignment, is treated as Gaussian noise with zero bias and a 0.2 deg standard deviation in the spacecraft's three body axes. The values of the navigation accuracy refer to the magnitude of the absolute position and velocity vectors in the RTN frame and are typical of an onboard GPS-based navigation system [34]. Further details about the navigation accuracy in the simulations are given in Appendix B. The initial state used for the orbit propagation is the same shown in Table 7, and the run time is one month. The reference orbit has been generated with the only inclusion of the GRACE GGM01S  $30 \times 30$  gravitational field in the forces model. The precise orbit determination (POD) ephemerides of the spacecraft TANGO of the PRISMA mission [18], the formation's target satellite, which flies in free motion, have been exploited to calibrate the atmospheric density model used for the simulations to have a high degree of realism. Figure 3 shows the time evolution of the difference between TANGO's real (POD) and reference orbital (RO) elements. Figure 3 includes also the difference between TANGO's orbit and an orbit propagated with the calibrated model.

### A. In-Plane Orbit Control

#### 1. Ideal Simulations Scenario

In these simulations, a constant atmospheric drag is the only perturbation force included in the orbit propagation model and no thruster, attitude, and navigation errors are included. The gravitational field model used for the orbit propagation is the GRACE GGM01S  $40 \times 40$ , whereas that used for the RO generation is the GRACE GGM01S  $30 \times 30$ . Figure 4 shows the REFE of the spacecraft, computed at the ascending node ( $\bar{u} = 0$ ), in case the orbit-control system is designed with the analytical algorithms of the AOK experiment [3,11] (AOK), Eq. (32) (linear), and Eq. (41) (LQR). Table 8 collects the parameters used for the design of the linear regulators [Eqs. (31), (44), and (45)]. The maneuver duty cycle imposed in all of the simulations was two orbital periods (i.e., the controllers could compute and command maneuvers once every third orbit). The execution of the maneuvers takes place at the ascending

**Table 3 PRISMA spacecraft physical properties**

Spacecraft physical property	MANGO	TANGO
Mass, kg	155.12	38.45
Drag area, m <sup>2</sup>	0.5625	0.2183
Drag coefficient	2.5	2.5
SRP effective area	0.5625	0.2183

**Table 4 Propagation parameters**

Propagation	Model
<i>Orbit</i>	
Earth gravitational field	GRACE GGM01S $40 \times 40$
Atmospheric density	Harris–Priester
Sun and Moon ephemerides	Analytical formulas [17]
Solid Earth, polar, and ocean tides	IERS
Relativity effects	First-order effects
Numerical integration method	Dormand–Prince
<i>RO</i>	
Earth gravitational field	GRACE GGM01S $30 \times 30$

**Table 5 Actuators accuracy**

Accuracy	Value
<i>Propulsion system</i>	
MIV	$7 \cdot 10^{-4}$ m/s
MIB	$7 \cdot 10^{-5}$ m/s
$\xi$	5%
<i>Attitude control</i>	
Mean	0 deg

**Table 6 Absolute navigation accuracy**

Navigation accuracy	Position	Velocity
Mean, m	3.04	$4.35 \cdot 10^{-3}$
$\sigma$ , m	1.6	$2.7 \cdot 10^{-3}$

node for the analytical controller, whereas it occurs following the rule of Eq. (35) for the linear regulators. Figure 4 shows how the phase difference vector component  $\delta L_\lambda$  is maintained in its control window by means of along-track maneuvers, which change the value of the orbit's semimajor axis. The guided time evolution of  $\delta a$  determines that of  $\delta u$  and thus the timing of the real with respect to the virtual spacecraft in passing at the ascending node [Eq. (4)]. The drift of the phase difference vector component  $\delta L_\phi$  is actually used to compensate the drift of  $\delta i_y$  in the control of  $\delta L_\lambda$  (Table 1). The linear and LQR regulators are able to control the eccentricity vector (and thus  $\delta h$ ) with the maneuvers' location rule of Eq. (35), whereas the analytical controller has no eccentricity vector control capability as it executes the maneuvers only at the orbit's ascending node. Figure 5 shows the orbital maneuvers commanded by the onboard controllers and executed by the spacecraft thrusters. Table 9 collects the control performance and the maneuvers budget. The goal of controlling  $\delta L_\lambda$  by means of along- and anti-along-track velocity increments is achieved with very similar performances by the three controllers. The main difference between the AOK analytical controller and the numerical regulators is that the AOK's maneuvers computation is based on a long-term prediction of  $\delta a$  highly dependent on the correct estimation of the semimajor axis decay rate  $da/dt$ . On the other hand, the linear regulators compute the orbital maneuvers with a pure feedback logic based on the values of the control gains. This fundamental difference between the two control strategies is demonstrated by examining Fig. 5. The linear and LQR regulators command groups of equal-sized consecutive maneuvers ( $\approx 8 \cdot 10^{-4}$  m/s) at nonregular time intervals, whereas the AOK control system commands larger maneuvers ( $\approx 2.5 \cdot 10^{-3}$  m/s) at a deterministic maneuvers cycle of two days. The AOK algorithm has an optimal control performance, in terms of control accuracy and  $\Delta v$  budget, if it has an accurate knowledge of the semimajor axis decay rate, as in the case of this simulation. The constant value of the atmospheric density used for the orbit propagation was, in fact, given as input to the AOK software.

**Table 7 Initial state**

Parameter	Value
<i>ECI state</i>	
X	-3,967,394.8566 m
Y	-289,822.105 m
Z	5,883,191.2151 m
$v_x$	-6,126.365 m/s
$v_y$	1,487.7675 m/s
$v_z$	-4,071.5062 m/s
<i>Mean orbital elements</i>	
a	7,130,522.2961 m
$e_x$	-0.004058
$e_y$	0.002774
$\dot{I}$	98.28 deg
$\Omega$	351.74 deg
U	123.38 deg

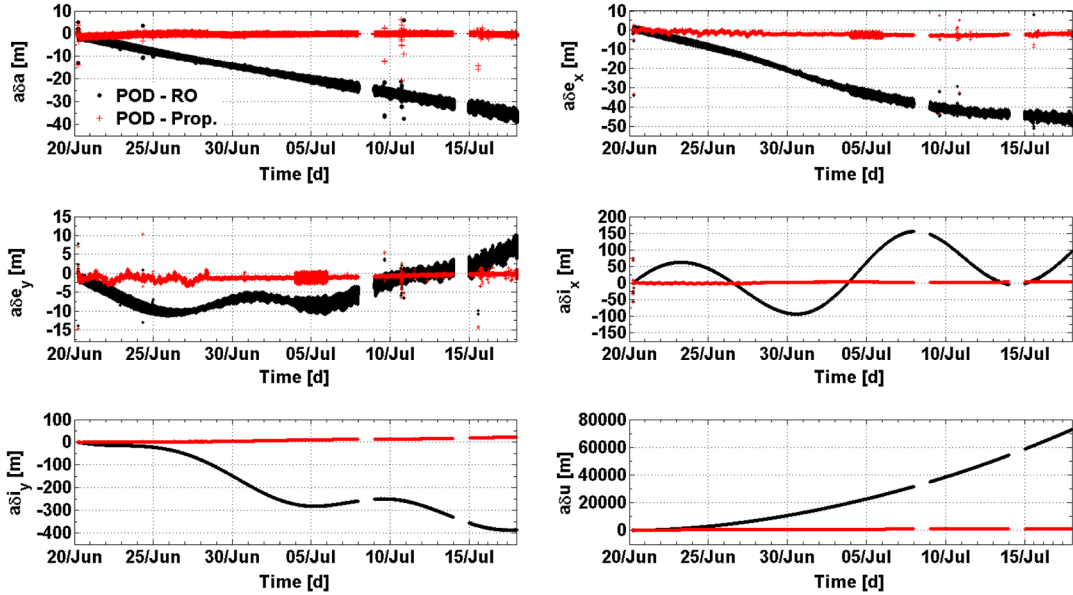


Fig. 3 Evolution in time of TANGO's orbital elements (POD) with respect to the reference and the propagated actual orbit.

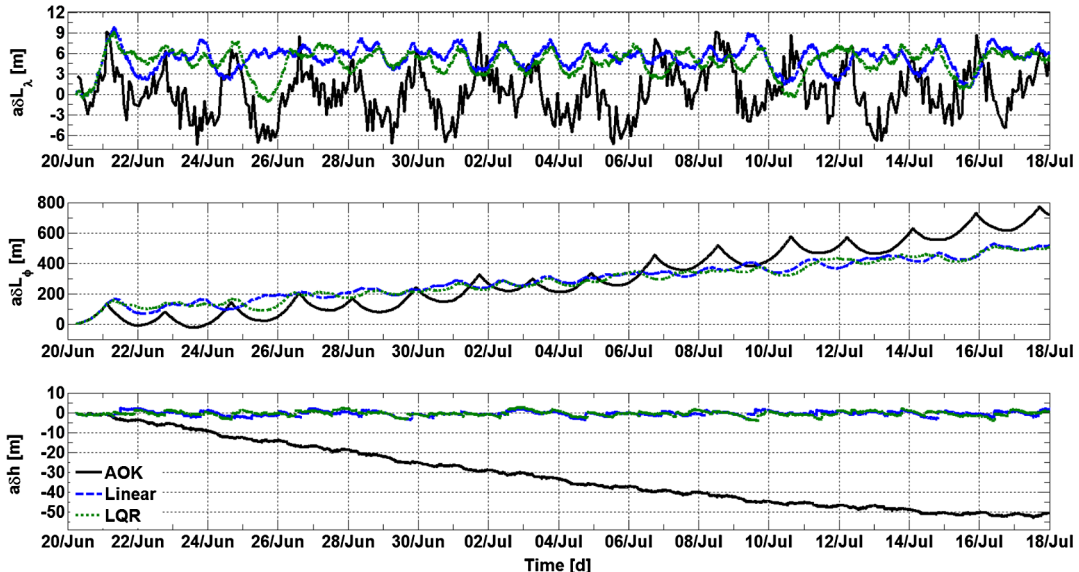


Fig. 4 Relative Earth-fixed elements (in-plane control).

## 2. Realistic Simulations Scenario

These simulations were run using the parameters in Tables 3–6. The regulators have been designed with the same parameters of Table 8, with the exception of the imposition of  $\delta L_{\lambda_{MAX}} = 15$  m for all of the regulators. Figure 6 shows the relative Earth-fixed elements of the spacecraft. A reference orbit acquisition based on the control of  $\delta L_\lambda$  [11] was also demonstrated. Table 10 collects the control performance and the maneuvers budget during the steady-state phase following the reference orbit acquisition. The degradation of the control performance with respect to the ideal case (Table 9) is mainly caused by the inclusion of the onboard navigation error in the simulation model. The placement of the maneuvers with the rule of Eq. (35), not optimized [33] from time to time, is not sufficient for a

strict control of the relative eccentricity vector because the solar radiation pressure perturbing force is this time included in the orbit's perturbation forces, and the orbit is not at frozen eccentricity. The AOK controller has, in this case, the additional disadvantage of inaccuracies in the onboard estimation of the atmospheric drag [3,11] and for this reason has a performance slightly worse than the linear regulators. The reliance of the AOK analytical controller on a correct onboard estimation of the atmospheric drag can be noticed by comparing Figs. 5 and 7 (top). The loss of accuracy in the onboard estimation of  $da/dt$  [11] entails the loss of determinism in the maneuver cycle. Table 11 offers an overview of the different pole placements in open and closed loop. The LQR is always able to find an optimal placement for all of the poles, while the linear in-plane regulator can place two poles only. Nevertheless, poles  $s_5$  and  $s_6$ , from which the control of  $\delta L_\lambda$  and  $d(\delta L_\lambda)/dt$  by means of along-track velocity increments depends upon, are placed in a similar way by both methods.

## B. In-Plane/Out-of-Plane Orbit Control

Figures 8 and 9 show the ROE and the REFE, respectively, of the spacecraft in case of in-plane/out-of-plane orbit control realized with the linear controller of Eq. (39) and in a realistic simulation scenario

Table 8 Regulator design parameters

	AOK	Linear	LQR
$\delta L_{\lambda_{MAX}}$ , m	5	10	10
$(d\delta L_\lambda/dt)_{MAX}$ , m/s	— —	100/86, 400	200/86, 400
$\Delta v_{R_{MAX}}$ , m/s	— —	— —	$10^{-6}$
$\Delta v_{T_{MAX}}$ , m/s	— —	$10^{-3}$	$10^{-3}$
$\Delta v_{N_{MAX}}$ , m/s	— —	— —	$10^{-6}$

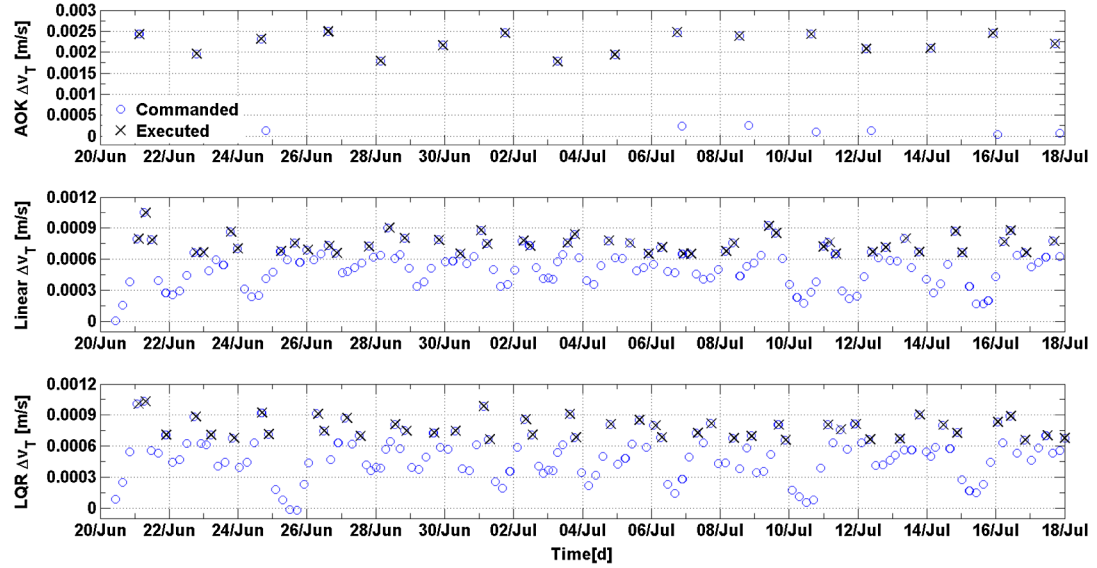


Fig. 5 Commanded and executed orbital maneuvers.

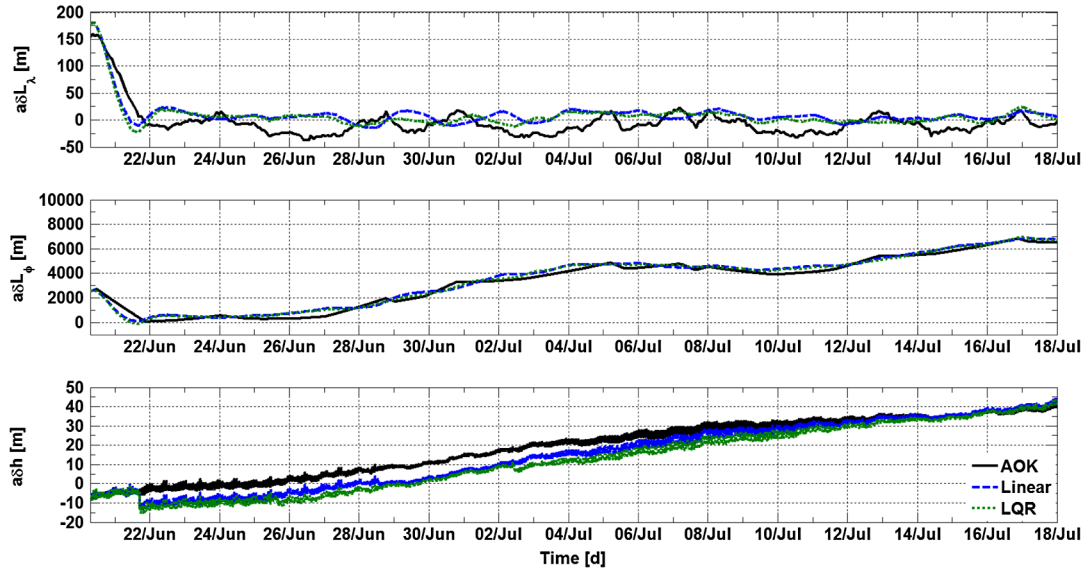


Fig. 6 Relative Earth-fixed elements (in-plane control).

(Tables 3–6). The gains were computed imposing the limits  $\delta L_{\lambda_{MAX}} = 10$  m,  $(d\delta L_\lambda/dt)_{MAX} = 100/86400$  m/s, and  $\delta i_{y_{MAX}} = 40$  m on the outputs and  $\Delta v_{T_{MAX}} = 1 \cdot 10^{-3}$  and  $\Delta v_{N_{MAX}} = 1.5 \cdot 10^{-2}$  m/s on the inputs. The value of  $\delta i_{y_{MAX}}$  was chosen to keep  $\delta L_\phi$  in a control window of 1500 m. The duty cycle imposed for the in-plane maneuver at the ascending node was four orbital periods (6 h)

and eight (12 h) for the out-of-plane maneuvers placed at  $u = \pi/2$ .

Unlike the case of the previous section, all the three states  $\delta a$ ,  $\delta i_y$ , and  $\delta u$  are controlled as all the poles are placed on the left of the imaginary axis (Table 11). As expected, the out-of-plane velocity increments allow the control of  $\delta L_\phi$  (Fig. 9). The same considerations

Table 9 Control performance and maneuvers budget with in-plane control

$\delta L_\lambda$ , m	Minimum	Maximum	Mean	$\sigma$	RMS	$\Delta v_T$ , m/s	Minimum	Maximum	Total
AOK	-7.4	9.2	0.18	3.6	3.6	AOK	0.0018	0.0025	0.0373
Linear	-0.6	9.9	5.3	1.7	5.6	Linear	0.0007	0.0011	0.0379
LQR	-1.2	9.1	4.8	1.8	5.1	LQR	0.0007	0.001	0.0374

Table 10 Control performance and maneuvers budget with in-plane control

$\delta L_\lambda$ , m	Minimum	Maximum	Mean	$\sigma$	RMS	$\Delta v_T$ , m/s	Minimum	Maximum	Total
AOK	-37.2	23.3	-9.8	13.5	16.7	AOK	-0.0078	0.0107	0.0942
Linear	-15.4	24.0	6.5	7.8	10.2	Linear	-0.0044	0.0112	0.0946
LQR	-13.3	24.5	3.9	7.5	8.4	LQR	-0.0049	0.0114	0.1228

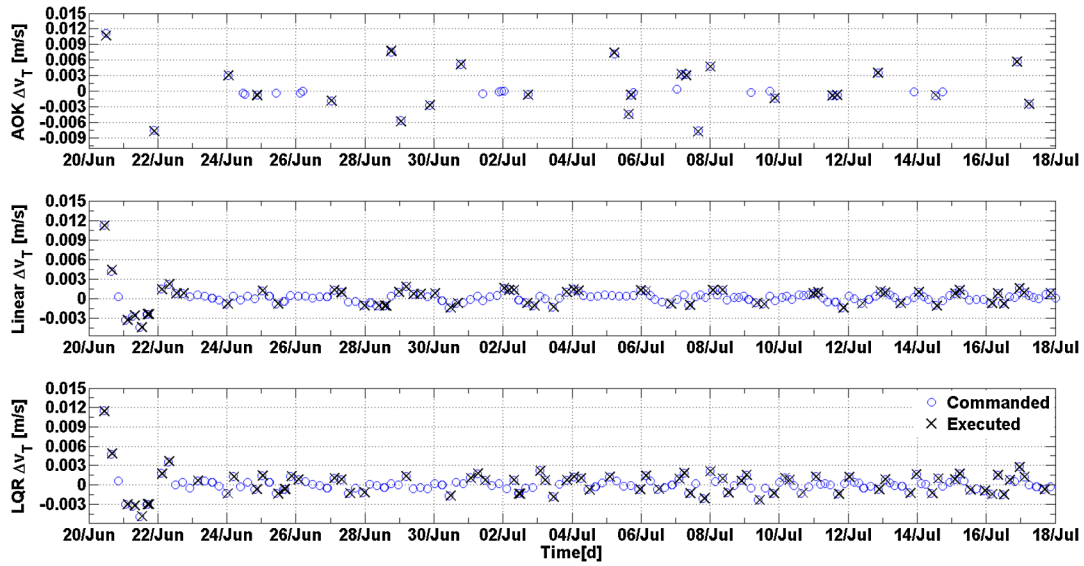
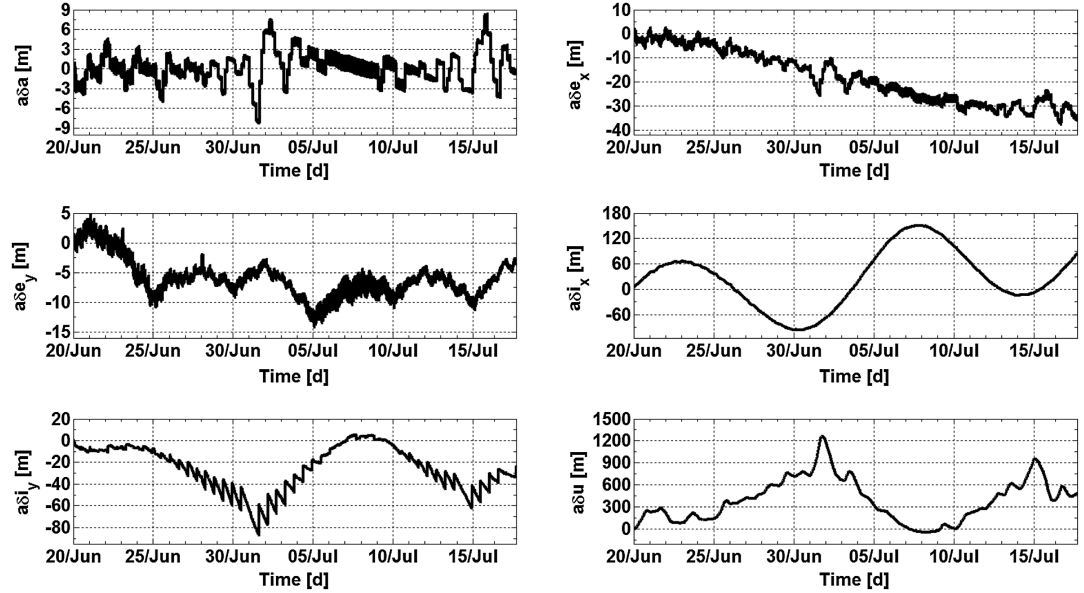
**Table 11 Poles**

	Open loop	Linear in-plane	LQR in-plane	In-plane/out-of-plane
$s_1$	0	— —	$-8.77 \cdot 10^{-10} - 8.78 \cdot 10^{-10}j$	— —
$s_2$	0	— —	$-8.77 \cdot 10^{-10} + 8.78 \cdot 10^{-10}j$	— —
$s_3$	$-2.38 \cdot 10^{-12}$	— —	$-3.16 \cdot 10^{-12} - 6.11 \cdot 10^{-7}j$	— —
$s_4$	$-5.71 \cdot 10^{-7}$	0	$-3.16 \cdot 10^{-12} + 6.11 \cdot 10^{-7}j$	$-3.56 \cdot 10^{-1}$
$s_5$	$-1.94 \cdot 10^{-5} + 4.35j$	$-1.61 \cdot 10^{-1}$	$-2.87 \cdot 10^{-1}$	$-1.61 \cdot 10^{-1}$
$s_6$	$-1.94 \cdot 10^{-5} - 4.35j$	$-7.72 \cdot 10^{-5}$	$-1.93 \cdot 10^{-4}$	$-1.15 \cdot 10^{-4}$

of the previous section regarding the in-plane control are valid here. In Fig. 8, one can also observe that  $\delta i_x$  is not influenced at all by  $\Delta v_N$  as the out-of-plane maneuvers are executed only when  $u = \pi/2$  [Eq. (A5)]. Figure 10 shows the orbital maneuvers commanded by the onboard controller and executed by the spacecraft thrusters. A regular maneuver cycle of the in-plane and out-of-plane maneuvers cannot be detected. Table 12 collects the control performance and the maneuvers budget. The in-plane control accuracy and cost is very similar to that of the simple linear controller of the previous section (Table 10). The out-of-plane  $\Delta v$  is 0.51 m/s, rather expensive compared to the in-plane maneuvers budget. These simulation results confirm that the in-plane and out-of-plane control problems can be treated separately in the design of the regulator.

## V. Conclusions

The problem of the autonomous absolute orbit control can be formalized as a specific case of two spacecraft in formation in which one, the reference, is virtual and affected only by the Earth's gravitational field. A new parametrization, the relative Earth-fixed elements, has been introduced for the translation of absolute orbit-control requirements in terms of relative orbit control. Methods developed for the formation keeping can thus be used for the orbit control of a single satellite. This approach allows also the straightforward use of modern control-theory numerical techniques for orbit control. Indeed, a bridge between the worlds of control theory and orbit control is built by this formalization. As a demonstration, a linear and a quadratic optimum regulator have been designed and

**Fig. 7 Commanded and executed orbital maneuvers.****Fig. 8 Relative orbital elements (in-plane and out-of-plane control).**

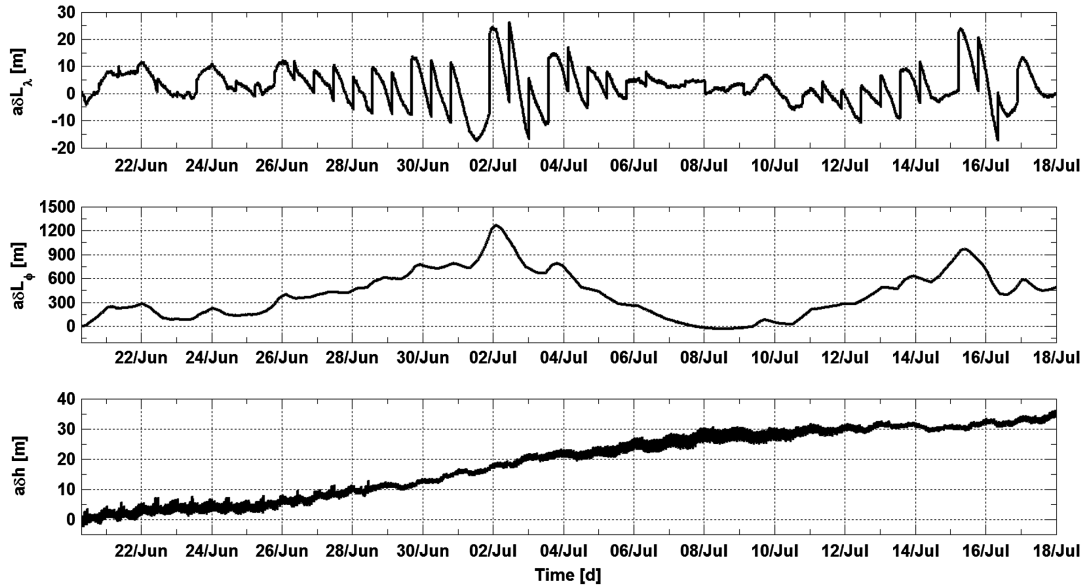


Fig. 9 Relative Earth-fixed elements (in-plane and out-of-plane control).

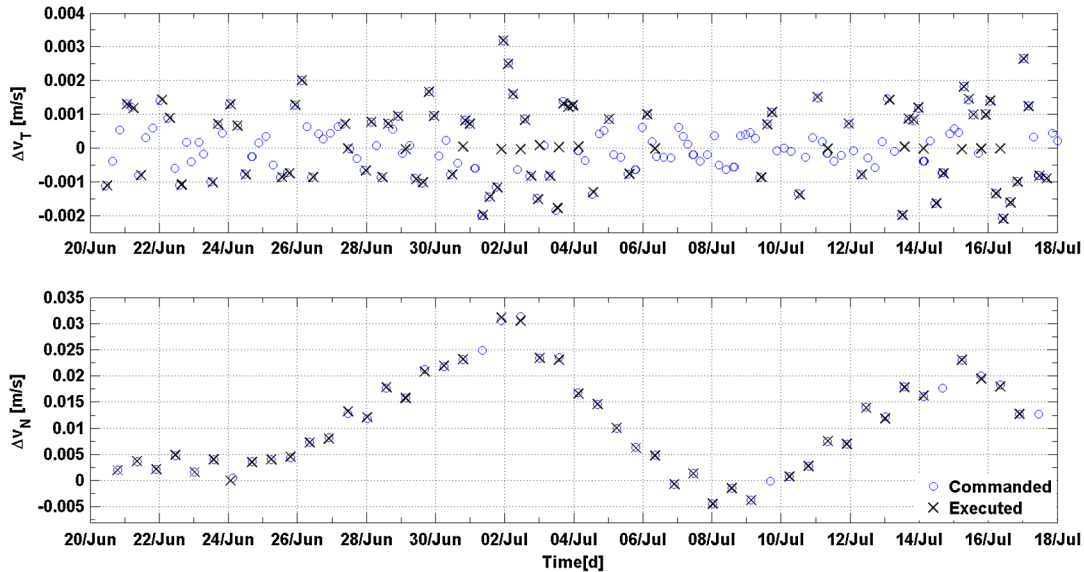


Fig. 10 Commanded and executed orbital maneuvers.

tested. These two numerical control methods have been compared, by means of numerical simulations, with an analytical algorithm that has been validated in flight with the autonomous orbit-keeping experiment on the PRISMA mission.

The main difference between these methods is that the maneuvers' computation by the analytical controller is based on a long-term orbit prediction, whereas the linear regulators compute the control actions with a pure feedback logic based on the values of the control gains. The accuracy of the orbit model therefore plays a critical role in the implementation of the analytical controller. For the implementation of the numerical feedback regulators, the critical issue is not the prediction accuracy of the model but its reliability in defining the stability conditions of the closed-loop system in the determination of the gains. The PRISMA analytical controller has demonstrated in-flight to be robust, cost-effective, and capable of

very good control accuracies. With the onboard availability of an accurate orbit model, this type of analytical controller has an optimal control performance in terms of accuracy and costs as well as a deterministic maneuver cycle, the duration of which depends on the size of the control window. On the other hand, the numerical regulators have a simpler flight software implementation and an enhanced flexibility given by the possibility of varying the type of onboard controller simply by uploading to the spacecraft different gain configurations. The type of control of these feedback systems is, in fact, entirely determined by the type and value of the gains.

The step forward is the design of a predictive control system with the same formal approach explained in this paper. This kind of numerical regulator can combine the advantages of the analytical and numerical orbit-control systems.

Table 12 Control performance and maneuvers budget with in-plane and out-of-plane control

$\delta L$ , m	Minimum	Maximum	Mean	$\sigma$	RMS	$\Delta v$ , m/s	Minimum	Maximum	Total
$\delta L_\lambda$	-17.5	26.3	2.4	6.7	7.1	$\Delta v_T$	-0.0021	0.0032	0.094
$\delta L_\varphi$	-153.9	1269.2	403.4	293.1	498.6	$\Delta v_N$	-0.0044	0.0312	0.51

## Appendix A: Linearized Orbit Model

### A1 Gravity Field

$$\tilde{\mathbf{A}}_g = \frac{3}{4} \left( \frac{R_E}{a} \right)^2 \frac{n J_2}{(1-e^2)^2} \begin{pmatrix} 0 \\ -(5 \cos^2 i - 1) e_y \\ (5 \cos^2 i - 1) e_x \\ 0 \\ -2 \cos i \\ 5 \cos^2 i - 1 + (3 \cos^2 i - 1) \sqrt{1 - e^2} \end{pmatrix} + \begin{pmatrix} 0 \\ 0 \\ 0 \\ 0 \\ 0 \\ n \end{pmatrix} \quad (\text{A1})$$

$$\mathbf{A}_g = \frac{3}{4} \left( \frac{R_E}{a} \right)^2 \frac{n J_2}{(1-e^2)^2} \begin{pmatrix} 0 & 0 & 0 & 0 & 0 & 0 \\ a_{g_{21}} & a_{g_{22}} & a_{g_{23}} & a_{g_{24}} & 0 & 0 \\ a_{g_{31}} & a_{g_{32}} & a_{g_{33}} & a_{g_{34}} & 0 & 0 \\ 0 & 0 & 0 & 0 & 0 & 0 \\ a_{g_{51}} & a_{g_{52}} & a_{g_{53}} & a_{g_{54}} & 0 & 0 \\ a_{g_{61}} & a_{g_{62}} & a_{g_{63}} & a_{g_{64}} & 0 & 0 \end{pmatrix} - \begin{pmatrix} 0 & \dots & 0 \\ \vdots & \ddots & \vdots \\ (3n/2a)a_R & \dots & 0 \end{pmatrix}$$

$$\begin{aligned} a_{g_{21}} &= \frac{7a_R}{2a} (5 \cos^2 i - 1) e_y & a_{g_{22}} &= -\frac{4(5 \cos^2 i - 1)}{(1-e^2)} e_x e_y & a_{g_{23}} &= -(5 \cos^2 i - 1) \left[ \frac{4e_y^2}{(1-e^2)} + 1 \right] \\ a_{g_{24}} &= 10e_y \sin i \cos i & a_{g_{31}} &= -\frac{7a_R}{2a} (5 \cos^2 i - 1) e_x & a_{g_{32}} &= (5 \cos^2 i - 1) \left[ \frac{4e_x^2}{(1-e^2)} + 1 \right] \\ a_{g_{33}} &= \frac{4(5 \cos^2 i - 1)}{(1-e^2)} e_x e_y & a_{g_{34}} &= -10e_x \sin i \cos i & a_{g_{51}} &= \frac{7a_R \cos i}{a \sin i_R} \\ a_{g_{52}} &= -\frac{8e_x \cos i}{(1-e^2) \sin i_R} & a_{g_{53}} &= -\frac{8e_y \cos i}{(1-e^2) \sin i_R} & a_{g_{54}} &= \frac{2 \sin i}{\sin i_R} \\ a_{g_{61}} &= -\frac{7a_R}{2a} [5 \cos^2 i - 1 + (3 \cos^2 i - 1) \sqrt{1 - e^2}] \\ a_{g_{62}} &= \frac{e_x}{(1-e^2)} [4(5 \cos^2 i - 1) + 3(3 \cos^2 i - 1) \sqrt{1 - e^2}] \\ a_{g_{63}} &= \frac{e_y}{(1-e^2)} [4(5 \cos^2 i - 1) + 3(3 \cos^2 i - 1) \sqrt{1 - e^2}] & a_{g_{64}} &= -2(5 + 3\sqrt{1 - e^2}) \sin i \cos i \end{aligned} \quad (\text{A2})$$

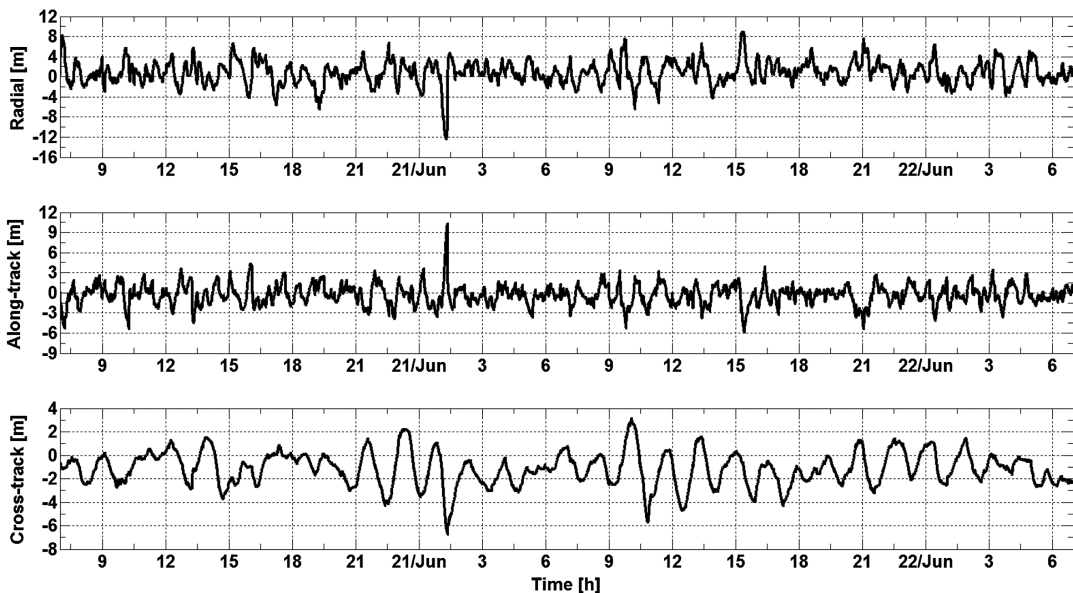


Fig. B1 Accuracy of the onboard estimated position in RTN (realistic simulations scenario).

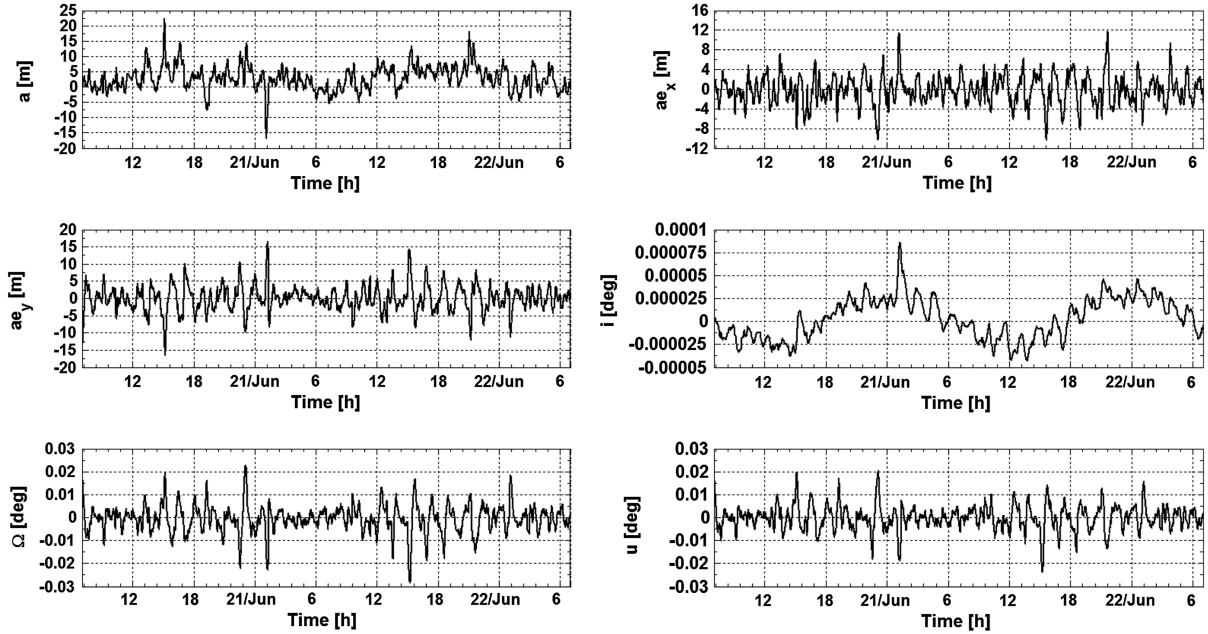


Fig. B2 Accuracy of the onboard estimated orbital elements (realistic simulations scenario).

Table B1 Navigation error (position and velocity in RTN)

	$R$ , m	$T$ , m	$N$ , m	Position (three-dimensional), m	$v_R$ , m/s	$v_T$ , m/s	$v_N$ , m/s	Velocity (three-dimensional), m/s
Mean	0.86	-0.30	-1.13	3.04	$3 \cdot 10^{-5}$	$-3.5 \cdot 10^{-5}$	$-2.3 \cdot 10^{-5}$	$4.35 \cdot 10^{-3}$
$\sigma$	2.32	1.51	1.42	1.60	$3 \cdot 10^{-3}$	$3.7 \cdot 10^{-3}$	$2 \cdot 10^{-3}$	$2.7 \cdot 10^{-3}$
RMS	2.47	1.54	1.81	3.43	$3 \cdot 10^{-3}$	$3.7 \cdot 10^{-3}$	$2 \cdot 10^{-3}$	$5.1 \cdot 10^{-3}$

## A2 Atmospheric Drag

$$\tilde{\mathbf{A}}_d = -\frac{A}{m} C_D \rho \begin{pmatrix} \sqrt{\mu a} \\ (e_x + \cos u) \sqrt{\mu/a} \\ (e_y + \sin u) \sqrt{\mu/a} \\ 0 \\ 0 \\ 0 \end{pmatrix} \quad (\text{A3})$$

$$\mathbf{A}_d = \frac{A}{m} C_D \rho \begin{pmatrix} a_{d_{11}} & 0 & 0 & 0 & 0 & 0 \\ a_{d_{21}} & a_{d_{22}} & 0 & 0 & 0 & a_{d_{26}} \\ a_{d_{31}} & 0 & a_{d_{33}} & 0 & 0 & a_{d_{36}} \\ 0 & 0 & 0 & 0 & 0 & 0 \\ 0 & 0 & 0 & 0 & 0 & 0 \\ 0 & 0 & 0 & 0 & 0 & 0 \end{pmatrix}$$

$$a_{d_{11}} = -\frac{1}{2a_R} \sqrt{\frac{\mu}{a}}$$

$$a_{d_{21}} = \frac{1}{2} n(e_x + \cos u) a_R$$

$$a_{d_{22}} = -\sqrt{\frac{\mu}{a}} \quad a_{d_{26}} = \sqrt{\frac{\mu}{a}} \sin u$$

$$a_{d_{31}} = \frac{1}{2} n(e_y + \sin u) a_R$$

$$a_{d_{33}} = -\sqrt{\frac{\mu}{a}}$$

$$a_{d_{36}} = -\sqrt{\frac{\mu}{a}} \cos u \quad (\text{A4})$$

Table B2 Navigation error (orbital elements)

	$a$ , m	$ae_x$ , m	$ae_y$ , m	$i$ , deg	$\Omega$ , m	$u$ , deg
Mean	2.78	-0.18	0.01	$3 \cdot 10^{-6}$	$-3.8 \cdot 10^{-4}$	$2.7 \cdot 10^{-5}$
$\sigma$	3.94	2.99	3.71	$2.2 \cdot 10^{-5}$	$6.1 \cdot 10^{-3}$	$5.6 \cdot 10^{-3}$
RMS	4.82	2.99	3.71	$2.2 \cdot 10^{-5}$	$6.1 \cdot 10^{-3}$	$5.6 \cdot 10^{-3}$

## A3 Control Matrix

$$\mathbf{B} = \frac{1}{n\Delta t} \begin{pmatrix} 0 & 2 & 0 \\ \sin u & 2 \cos u & 0 \\ -\cos u & 2 \sin u & 0 \\ 0 & 0 & \cos u \\ 0 & 0 & \sin u \\ -2 & 0 & -\sin u / \tan i \end{pmatrix}, \quad \Delta t = 1s \quad (\text{A5})$$

## Appendix B: Navigation Accuracy

Figures B1 and B2 and Tables B1 and B2 show the accuracy of the onboard estimated absolute position in the RTN orbital frame and of the orbital elements in the realistic simulations scenario.

## References

- [1] Wertz, J. R., and Gurevich, G., "Applications of Autonomous On-Board Orbit Control," *11th AAS/AIAA Space Flight Mechanics Meeting*, AAS Paper 2001-238, Feb. 2001.
- [2] Bonaventure, F., Baudry, V., Sandre, T., and Gicquel, A.-H., "Autonomous Orbit Control for Routine Station Keeping on a LEO Mission," *Proceedings of the 23rd International Symposium on Space Flight Dynamics*, Pasadena, CA, Oct.–Nov. 2012.
- [3] De Florio, S., and D'Amico, S., "The Precise Autonomous Orbit Keeping Experiment on the Prisma Mission," *Journal of the Astronautical Sciences*, Vol. 56, No. 4, 2008, pp. 477–494.  
doi:10.1007/BF03256562

- [4] Garulli, A., Giannitrapani, A., Leonardi, M., and Scortecci, F., "Autonomous Low-Earth-Orbit Station-Keeping with Electric Propulsion," *Journal of Guidance, Control, and Dynamics*, Vol. 34, No. 6, Nov.–Dec. 2011, pp. 1683–1693.  
doi:10.2514/1.52985
- [5] Julien, E., and Lamy, A., "Out-of-Plane Autonomous Orbit Control," *Journal of Aerospace Engineering, Sciences and Applications*, Vol. 4, No. 3, 2012, pp. 28–40.  
doi:10.7446/jaes.0403.03
- [6] Königsmann, H. J., Collins, J. T., Dawson, S., and Wertz, J. R., "Autonomous Orbit Maintenance System," *Acta Astronautica*, Vol. 39, Nos. 9–12, 1996, pp. 977–985.  
doi:10.1016/S0009-5765(97)00084-2
- [7] Galski, R. L., and Orlando, V., "Autonomous Orbit Control Procedure, Using a Simplified GPS Navigator and a New Longitude Phase Drift Prediction Method, Applied to the CBERS Satellite," *Journal of Aerospace Engineering, Sciences and Applications*, Vol. 4, No. 3, July–Sept. 2012, pp. 54–61.  
doi:10.7446/jaes.0403.05
- [8] Orlando, V., and Kuga, H. K., "A Survey of Autonomous Orbit Control Investigations at INPE," *Proceedings of the 17th International Symposium on Space Flight Dynamics*, Moscow, June 2003.
- [9] Plam, Y., Allen, R. V., Wertz, J. R., and Bauer, T., "Autonomous Orbit Control Experience on TacSat-2 Using Microcosm's Orbit Control Kit (OCK)," *31st Annual AAS Guidance and Control Conference*, AAS Paper 2008-008, Feb. 2008.
- [10] Lamy, A., Julien, E., and Flamenbaum, D., "Four Year Experience of Operational Implementation of Autonomous Orbit Control: Lessons Learned, Feedback and Perspectives," *Proceedings of the 21st International Symposium on Space Flight Dynamics*, Toulouse, France, 2009.
- [11] De Florio, S., D'Amico, S., and Radice, G., "Flight Results of the Precise Autonomous Orbit Keeping Experiment on the Prisma Mission," *Journal of Spacecraft and Rockets*, Vol. 50, No. 3, 2013, pp. 662–674.  
doi:10.2514/1.A32347
- [12] Gurfil, P., and Kholshevnikov, K. V., "Manifolds and Metrics in the Relative Spacecraft Motion Problem," *Journal of Guidance, Control, and Dynamics*, Vol. 29, No. 4, 2006, pp. 1004–1010.  
doi:10.2514/1.15531
- [13] Alfriend, K.T., Vadali, S. R., Gurfil, P., How, J. P., and Breger, L. S., *Spacecraft Formation Flying: Dynamics, Control and Navigation*, Elsevier Astrodynamics Series, Elsevier, Oxford, England, U.K., 2010, Chap. 6.
- [14] Schaub, H., "Relative Orbit Geometry Through Classical Orbit Element Differences," *Journal of Guidance, Control, and Dynamics*, Vol. 27, No. 5, Sept.–Oct. 2004, pp. 839–848.  
doi:10.2514/1.12595
- [15] Micheau, P., "Orbit Control Techniques for LEO Satellites," *Spaceflight Dynamics*, Vol. 1, Cepadues-Editions, Toulouse, France, 1995, pp. 739–902.
- [16] D'Amico, S., Arbinger, C., Kirschner, M., and Campagnola, S., "Generation of an Optimum Target Trajectory for the TerraSAR-X Repeat Observation Satellite," *Proceedings of the 18th International Symposium on Space Flight Dynamics*, Munich, Oct. 2004.
- [17] Montenbruck, O., and Gill, E., *Satellite Orbits: Model, Methods, and Applications*, Springer-Verlag, Heidelberg, Germany, 2000, Chaps. 3, 5.
- [18] Bodin, P., Noteborn, R., Larsson, R., Karlsson, T., D'Amico, S., Ardaens, J.-S., Delpech, M., and Berge, J.-C., "The Prisma Formation Flying Demonstrator: Overview and Conclusions from the Nominal Mission," *Proceedings of the 35th Annual AAS Guidance and Control Conference*, AAS Paper 2012-072, Feb. 2012.
- [19] D'Amico, S., Bodin, P., Delpech, M., and Noteborn, R., "PRISMA," *Distributed Space Missions for Earth System Monitoring*, Vol. 31, Space Technology Library, Springer, New York, 2013, pp. 599–637.
- [20] Friedland, B., *Control System Design: An Introduction to State Space Methods*, McGraw-Hill, New York, 1986, pp. 14–111, 190–221, 337–377, Chaps. 2, 3, 5, 9.
- [21] Kirk, D. E., *Optimal Control Theory: An Introduction*, Prentice-Hall, Englewood Cliffs, NJ, 1970, pp. 1–47, 184–310.
- [22] Kahle, R., Kazeminejad, B., Kirschner, M., Yoon, Y., Kiehlin, R., and D'Amico, S., "First In-Orbit Experience of TerraSAR-X Flight Dynamics Operations," *Proceedings of the 20th International Symposium on Space Flight Dynamics*, Annapolis, MD, Sept. 2007.
- [23] Martin, M. A., Shurmer, I., and Marc, X., "Sentinel-1: Operational Approach to the Orbit Control Strategy," *Proceedings of the 23rd International Symposium on Space Flight Dynamics*, Pasadena, CA, Oct.–Nov. 2012.
- [24] De Florio, S., and D'Amico, S., "Max-Path Unit Tests of the PRISMA Flight Software v. 6.0.0," DLR, German Aerospace Center, Rept. PRISMA-DLR-TN-17, Cologne, Germany, 2007.
- [25] D'Amico, S., De Florio, S., and Yamamoto, T., "Offline and Hardware-in-the-Loop Validation of the GPS-Based Real-Time Navigation System for the PRISMA Formation Flying Mission," *Proceedings of the 3rd International Symposium on Formation Flying, Missions and Technology*, ESA Paper SP-654, Paris, April 2008.
- [26] D'Amico, S., Ardaens, J.-S., and Larsson, R., "Spaceborne Autonomous Formation Flying Experiment on the PRISMA Mission," *Journal of Guidance, Control and Dynamics*, Vol. 35, No. 3, 2012, pp. 834–850.
- [27] Brouwer, D., "Solution of the Problem of Artificial Satellite Theory Without Drag," *Astronomical Journal*, Vol. 64, No. 1274, 1959, pp. 378–397.  
doi:10.1086/107958
- [28] Walter, H. G., "Conversion of Osculating Orbital Elements into Mean Elements," *Astronomical Journal*, Vol. 72, No. 8, Oct. 1967, pp. 994–997.  
doi:10.1086/110374
- [29] Schaub, H., and Junkins, J. L., "Analytical Mechanics of Space Systems," AIAA Education Series, AIAA, Reston, VA, 2003, pp. 525, 649–651, 693–698.
- [30] D'Amico, S., and Montenbruck, O., "Proximity Operations of Formation-Flying Spacecraft Using an Eccentricity/Inclination Vector Separation," *Journal of Guidance, Control, and Dynamics*, Vol. 29, No. 3, May–June 2006, pp. 554–563.
- [31] Clohessy, W. H., and Wiltshire, R. S., "Terminal Guidance System for Satellite Rendezvous," *Journal of Aerospace Sciences*, Vol. 27, No. 9, 1960, pp. 653–658.
- [32] Liu, J., "Satellite Motion About an Oblate Earth," *AIAA Journal*, Vol. 12, No. 11, 1974, pp. 1511–1516.  
doi:10.2514/3.49537
- [33] D'Amico, S., Kirschner, M., and Arbinger, C., "Precise Orbit Control of LEO Repeat Observation Satellites with Ground-in-the-Loop," DLR, German Aerospace Center, TN-04-05, Oberpfaffenhofen, Germany, 2004.
- [34] Ardaens, J.-S., D'Amico, S., and Montenbruck, O., "Final Commissioning of the Prisma GPS Navigation System," *Journal of Aerospace Engineering, Sciences and Applications*, Vol. 4, No. 3, July–Sept. 2012, pp. 104–118.  
doi:10.7446/jaes.0403.10